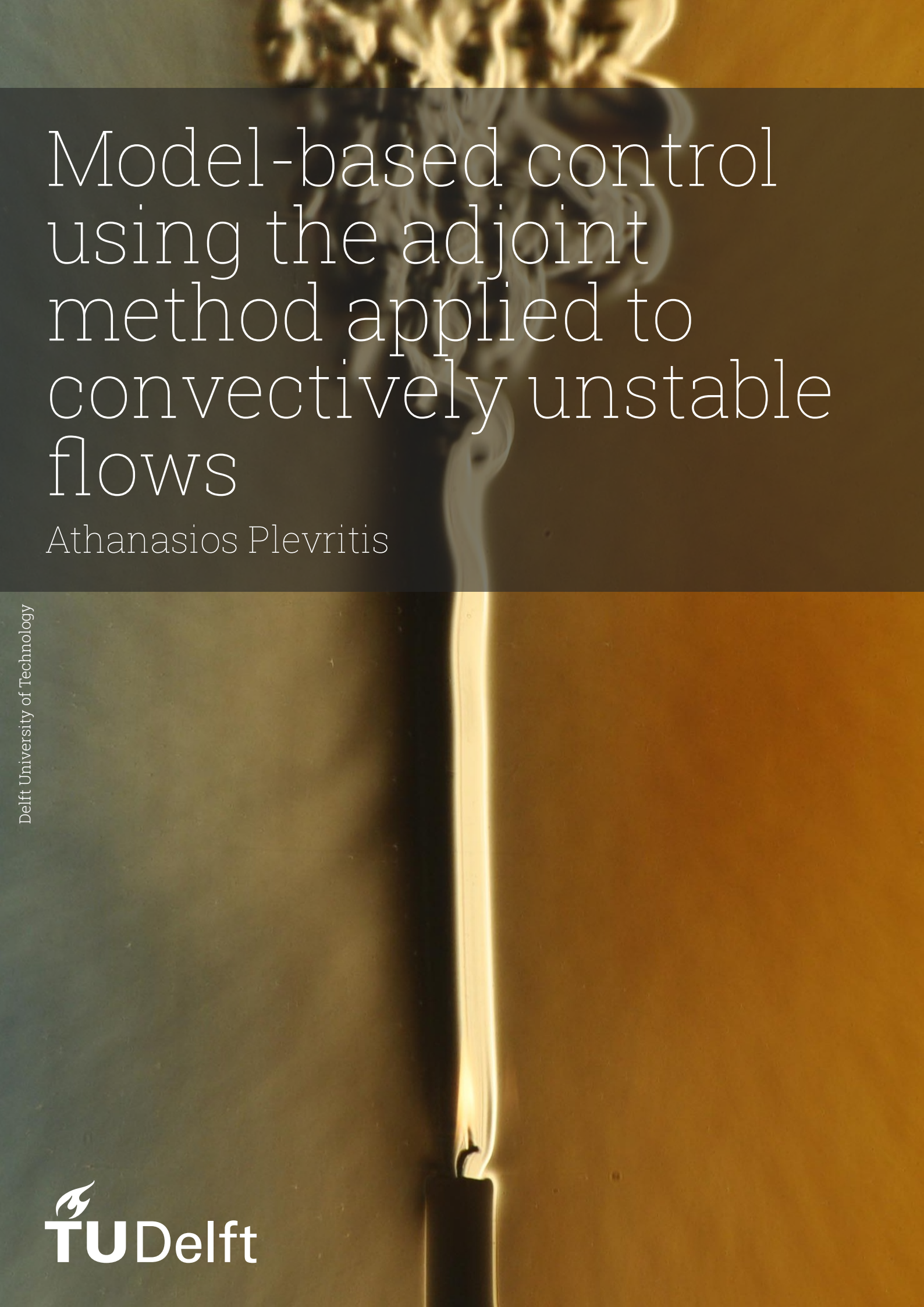

Model-based control using the adjoint method applied to convectively unstable flows

Athanasios Plevritis

Delft University of Technology

TU Delft

Model-based control using the adjoint method applied to convectively unstable flows

by

Athanasios Plevritis

to obtain the degree of Master of Science

at the Delft University of Technology,

to be defended publicly on Monday September 29, 2025 at 9:00 AM.

Student number:	5978742	
Thesis committee:	Dr. R. P. Dwight,	TU Delft, supervisor
	Dr. S. J. Hulshoff,	TU Delft
	Dr. N. A. K. Doan,	TU Delft

Cover:	Settles, Gary. 2009. Laminar-Turbulent Transition. Photograph. Wikimedia Commons. March 10, 2009. Licensed CC BY-SA 3.0. `https://commons.wikimedia.org/wiki/File:Laminar-turbulent_transition.jpg`
Style:	TU Delft Report Style, with modifications by Daan Zwaneveld

An electronic version of this thesis is available at `http://repository.tudelft.nl/`.

TU Delft

Acknowledgments

This thesis marks the end of my 2-year long post-graduate studies at TU Delft.

I would like to express my deepest gratitude to my supervisor, Richard Dwight, for their invaluable guidance, encouragement, and support throughout the course of my thesis.

I am also sincerely thankful to Srinivas Vellala, whose assistance, advice, and patience have been instrumental in helping me overcome many challenges during my research.

Finally, I wish to express my heartfelt thanks to my family for their love, understanding, and encouragement.

Athanasios Plevritis
Delft, September 2025

Abstract

Flow control plays a vital role in improving efficiency in aerospace, maritime, and energy systems by delaying transition to turbulence and suppressing instabilities such as Tollmien–Schlichting waves. This work uses the Kuramoto–Sivashinsky (KS) equation as a model to study convective instabilities in boundary layers. A finite-difference discretization yields a state-space formulation, enabling systematic application of control strategies. Linear Quadratic Regulator (LQR) and adjoint-based optimization methods are developed to minimize flow perturbations. Results show LQR effectively suppresses disturbances, while adjoint-based control scales efficiently to nonlinear cases, highlighting promising avenues for future turbulence management.

Contents

List of Figures

List of Tables

1

Introduction

Flow control represents a critical area of research in fluid dynamics, with significant implications for enhancing efficiency and performance across aerospace, maritime, and energy systems. The ability to delay laminar-to-turbulent transition or suppress undesirable flow instabilities - such as Tollmien–Schlichting (TS) waves - can lead to substantial reductions in skin friction drag, fuel consumption, and operational costs [1], [2]. Even minor improvements can result in billions of dollars in annual savings for the transport industry [3]. Traditional control strategies often rely on empirical or heuristic approaches, but there is growing interest in model-based methods that leverage modern control theory and numerical optimization to address these complex challenges more systematically [4], [5].

Model-based methods can be divided into iterative and direct methods. The main difference between the iterative (adjoint-based) and direct (Riccati-based) methods lies in the state chosen for linearization. In the iterative approach, linearization occurs around an actual system trajectory. At each step, a new linearization of the governing equations is performed. Conversely, the direct method involves performing a single linearization around a typical mean flow condition, which may also act as a solution to the governing equations. In small scale problems, direct methods are undoubtedly the most effective way to tackle any flow control problem. Nevertheless, the ultimate goal in a real-world flow control problem is to use the full non-linear Navier-Stokes as the model. This creates an enormous demand for computational power and memory capacity, as a typical order of magnitude of the degrees of freedom that are needed for such cases lays around 10^5. This work establishes the feasibility of these methods, paving the way for their eventual application in real-world scenarios.

The methodology of this work centers on the use of the linear and nonlinear Kuramoto–Sivashinsky (KS) equation as a model problem to emulate the convective instability behavior of boundary layer flows [6], [7]. A finite-difference discretization is employed to transform the partial differential equation into a state-space formulation. Both Linear Quadratic Regulator (LQR) [8] and adjoint-based optimization techniques are applied to compute control inputs that minimize flow perturbations.

Chapter 2 provides a theoretical background and literature review, covering flow instability mechanisms, transition to turbulence, classical and modern flow control techniques. Chapter 3 details the mathematical framework of the KS equation, its linearization, state-space representation, and the formulation of both LQR and adjoint-based control strategies. Chapter 4 presents and discusses the results: first, the performance of the LQR controller in suppressing perturbations; second, the application of the adjoint method to the linear KS equation and its comparison with Riccati-based control; and third, the extension to the nonlinear KS equation, highlighting the scalability of the adjoint approach. The thesis concludes with a summary of findings and suggestions for future work.

2

Theoretical background - Literature review

2.1 The importance of flow control

The ability to alter flow patterns to achieve particular objectives is of paramount importance across various domains. For example, the global maritime industry consumes approximately 2.1 billion barrels of oil each year [9]. Even a minor decrease in the overall drag can result in billions of dollars in savings annually, besides aiding in the preservation of the planet's limited resources. Moreover, reduced drag can enhance speed, range, and endurance for commercial airliners. In fluid mechanical systems, it is common to aim for effects such as reducing structural vibrations, noise emissions, and surface heat exchange, which are generally associated with a decrease in flow-field unsteadiness. Meanwhile, enhancing mixing and combustion efficiency is an issue mostly related to an appropriate increase in flow-field unsteadiness. Unsurprisingly, there has been significant interest in modifying flows to achieve these results for more than a century.

Today, the term ”flow control” is commonly used to describe a variety of techniques appropriate to different contexts. At its core, it involves methods that modify or impact fluid flow to achieve specific characteristics. More specifically, it can pertain to the application of control and systems theory to the Navier-Stokes equations. Between these points, there are several interpretations, including those that leverage physical intuition and empirical modifications informed by a designer's understanding of fluid dynamics. While these intuitive methods have been successful and continue to play a vital role, utilizing model-based control theory presents new possibilities for addressing complex challenges in fluid mechanics.

Reducing these viscous drag losses in various engineering fields can potentially result in significant economic savings, potentially amounting to billions of dollars [3]. Managing flow to reduce viscous drag can additionally impact a variety of other drawbacks and losses such as pressure drag due to displacement thickness, wave drag of hydrodynamic origin, heat and mass transfer at the wall, fluctuations in wall pressure, as well as the size of wakes and the level of turbulence (Table 2.1).

Skin Friction Drag Contribution	**Application**
50%	Transport aircraft and surface ships
30–40%	High-speed aircraft, missiles, and aerospace planes
70%	Underwater bodies
100%	Pipelines

Table 2.1: Skin friction drag contribution for various applications [1].

Consequently, it is possible to achieve decreased requirements for heat and sound insulation, smaller and lighter heat exchangers, prevention of cavitation, and enhanced sensor performance. Reducing

drag will enhance range, decrease fuel volume and weight, and shrink both the vehicle's size and weight, while also boosting speed and payload capacity [10].

The central goal of drag reduction studies in external flows is to aid in developing vehicle designs that consume considerably less fuel [11]. Drag can be split into three different components, pressure or form drag, skin friction drag and lift induced drag. One of the biggest contributors to drag is the pressure or form drag, which becomes especially problematic when flow separation happens [12]. The physics behind this drag component involves the impact of viscosity on the pressure field of an ideal or inviscid flow. Even when the flow remains attached, a modest level of pressure drag is present. This is due to the viscosity-induced displacement of the flow. Nonetheless, when flow separation takes place, this drag component escalates dramatically [13]. Consequently, the primary focus for the regulation and reduction of drag for optimal efficiency is to prevent flow separation. The two remaining components of drag, namely skin-friction drag and lift-induced drag, are generally of a similar magnitude and considerably smaller compared to the pressure or form drag, except when dealing with attached flow, where pressure drag is also minor. Skin-friction drag arises from the no-slip boundary condition on a surface and can manifest either in a laminar or turbulent flow. Indeed, sustaining laminar flow at elevated Reynolds numbers is a well-known and presently popular method for reducing skin friction [14], [15]. The different drag mechanisms interact with each other, and since laminar flow separates more readily, it can be beneficial to intentionally transition the flow to a turbulent state, thereby preventing the substantial pressure drag that occurs with flow separation. The additional drag component, known as drag due to lift, arises from the flow spillage on lifting surfaces as it moves between areas of high and low pressure. This work focuses on an active control approach for reducing the skin friction drag.

Earlier studies focused on reducing ”form” or ”pressure” drag and minimizing surface roughness have lowered the zero-lift drag coefficient of a majority of aerial and underwater vehicles to exceptionally low levels, approaching those typical of attached viscous flow [1]. Indeed, viscous drag, is now regarded as a significant obstacle to the enhanced optimization not only in aerodynamic and hydrodynamic structures but also on other areas that include interactions between fluids and solid surfaces.

On a flat surface, the average skin friction within a turbulent boundary layer is usually approximately ten times greater than that found in a laminar boundary layer [2]. The manner in which transition occurs is dependent upon the intensity of external disturbances affecting the boundary layer. In conditions where the ambient turbulence is minimal and the flow downstream has sufficiently progressed, transition typically initiates through the gradual intensification of small perturbations referred to as Tollmien–Schlichting (TS) waves. These perturbations eventually amplify in scale and experience nonlinear interactions, resulting in a cascade down into smaller turbulent formations. On the other hand, when more intense disruptions appear in the free stream, the traditional development of TS waves is circumvented. Instead, the transition is activated by the algebraic growth of extended formations known as streaks along the direction of the flow. Postponing the transition can be accomplished by inhibiting the formation of TS waves or streaks, thus averting their subsequent breakdown. This method also allows for the application of linear systems theory in designing flow control strategies.

2.2 Laminar-Turbulent transition and Tollmien–Schlichting wave formation

As the Reynolds number is increased, both internal flows through pipes and channels and external boundary–layers flows past bodies exhibit a noticeable change from a laminar flow form to a turbulent flow form. The laminar–turbulent transition is a stability problem, based on the idea that laminar flow is acted on by some small perturbations, such as those which could arise due to the pipe entrance geometry or the roughness of a plate. At small Reynolds numbers, i.e. at large values of viscosity, the damping action of the viscosity is large enough to ensure that these small perturbations die away again. It is only at large enough Reynolds numbers that the damping due to the viscosity is no longer sufficient, so that the disturbances are intensified and thus eventually initiate the transition to turbulence.

In flows involving boundary layers around solid bodies - such as an aircraft's airfoil - the overall flow behavior and the resulting forces on the surface are highly influenced by whether the boundary layer is laminar or turbulent. The transition between these two states depends on several factors, with key influences including the Reynolds number, external pressure distribution, surface roughness, and the

turbulence level in the surrounding flow. As the flow progresses downstream, the laminar flow area is replaced by axisymmetric waves known as Tollmien–Schlichting waves. These waves trigger a transition to turbulent flow, characterized by the formation of a distinct three-dimensional structure. This part of the flow is known as the ”transition region”.

A typical case where the laminar–turbulent transition can be observed is a flat plate at zero incidence. For the laminar boundary layer plate showed us that the boundary–layer thickness grows with $\sqrt{x}$, where x is the distance from the leading edge. The transition from the laminar to the turbulent boundary layer was first investigated by J.M. Burgers [16] and B.G. Van der Hegge Zijnen [17]. Close to the leading edge of the plate, the boundary layer is initially always laminar but further downstream it then becomes turbulent.

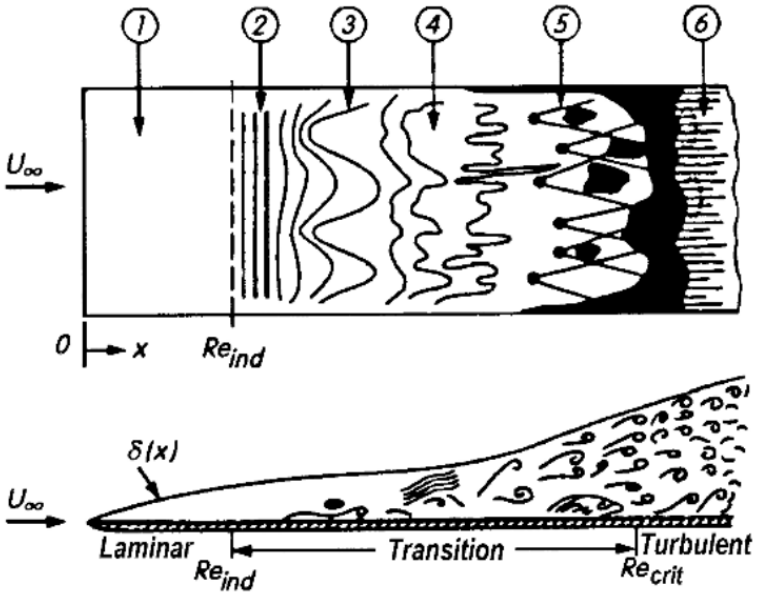

Figure 2.1: Sketch of laminar–turbulent transition in the boundary layer on a flat plate at zero incidence, after F.M. White (1974). (1) Stable laminar flow, (2) Unstable Tollmien – Schlichting waves, (3) Three-dimensional waves and vortex formation (Λ-structures), (4) Vortex decay, (5) Formation of turbulent spots, (6) Fully turbulent flow. [2]

The basic sketch in Figure 2.1 illustrates the principal experimental findings on transition. Two-dimensional Tollmien-Schlichting waves are superimposed onto the laminar boundary-layer flow at the indifference Reynolds number Re_{ind}, as described by primary stability theory. As a result of secondary instabilities, three-dimensional disturbances are introduced further downstream, resulting in the formation of a characteristic Λ-structures. Subsequently, the Λ-vortices are succeeded by turbulent spots, triggering the transition to a fully turbulent boundary-layer flow. When $Re_x = Re_{x\ crit}$, the transition is finalized, and the flow becomes fully turbulent downstream.

Figure 2.1 illustrates that the transition is accompanied by a significant rise in the boundary-layer thickness. In a laminar boundary layer, the non-dimensional boundary-layer thickness $\delta/\sqrt{\nu x/U_\infty}$ remains constant at a value near 5 [2]. Figure 2.2 depicts this non-dimensional boundary-layer thickness as a function of the Reynolds number based on the length x, specifically $\mathrm{Re}_x = U_\infty x/\nu$. When $\mathrm{Re}_x \geq 3 \cdot 10^5$, a notable increase in the boundary-layer thickness is observed.

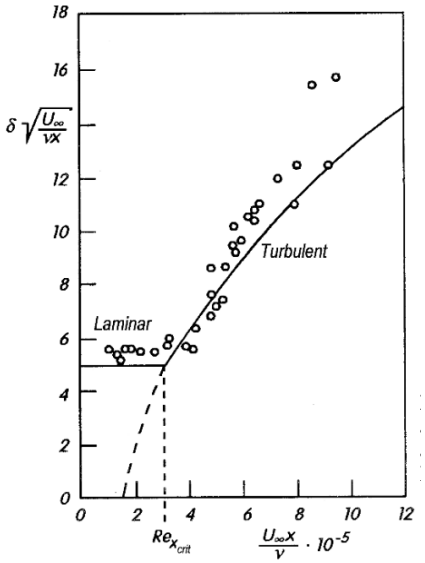

Figure 2.2: Dependence of the boundary-layer thickness on the distance along a plate at zero incidence, after M. Hansen (1928). Fictitious turbulent origin at $\mathrm{Re}_x = 1.5 \times 10^5$ [2]

Additionally, there is an evident modification in the time-averaged velocity profile. Figure 2.3 illustrates the velocity profile within a transitional region ranging from approximately $\mathrm{Re}_x = 3 \cdot 10^6$ to $4 \cdot 10^6$ for a flow with minimal turbulence intensity. In this region, the velocity distribution transitions from the Blasius profile characteristic of a laminar plate boundary layer to that of a fully turbulent plate boundary layer.

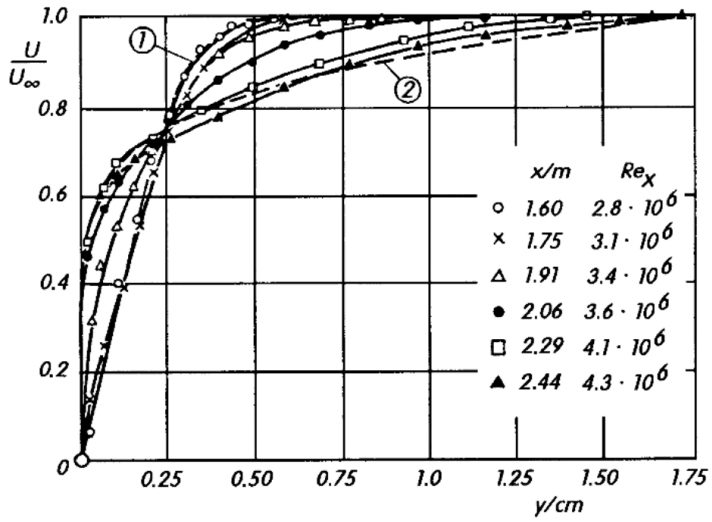

Figure 2.3: Velocity profile of the plate boundary layer close to the laminar-turbulent transition, after measurements by G.B. Schubauer and P.S. Klebanoff (1955). Outer velocity $U_\infty = 27$ m/s; outer flow turbulence intensity $Tu = 3 \cdot 10^{-4}$. (1) laminar, Blasius profile; (2) turbulent profile , $\delta = 17$ mm [2]

Along with the reorganization of the velocity distribution in the transition region, a significant decrease in the shape factor $H_{12} = \delta_1/\delta_2$ occurs, as shown in Figure 2.4. For the plate boundary layer, the shape factor decreases from $H_{12} \approx 2.6$ in the laminar region to $H_{12} \approx 1.4$ in the turbulent region.

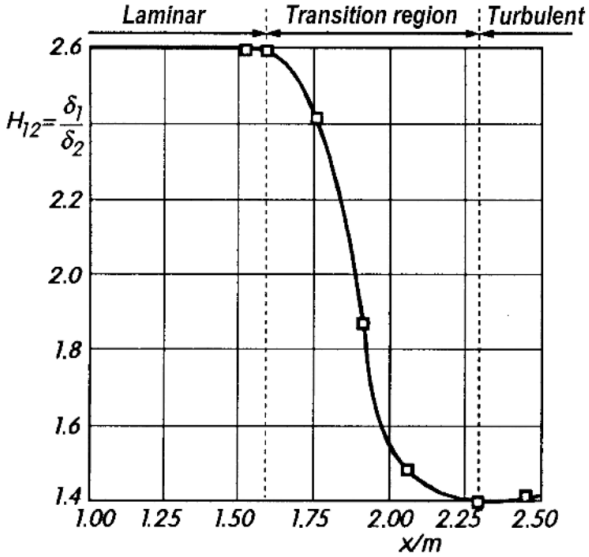

Figure 2.4: Change of the shape factor $H_{12} = \delta_1/\delta_2$ for the plate boundary layer close to the laminar-turbulent transition, after measurements by G.B. Schubauer and P.S. Klebanoff (1955) [2]

There is also a significant change in the drag (in this case friction drag) during the laminar–turbulent transition. While the friction drag D for laminar flow is proportional to $U_\infty^{3/2}$, for turbulent flow $D \sim (U_\infty / \ln U_\infty)^2$.

Slender bodies especially experience significant effects from pressure gradients on boundary-layer flow, affecting the transition region's position. Decreasing pressure (accelerated flow) keeps the boundary layer laminar, while slight pressure increases trigger transition. For slender bodies like airfoils, optimizing body shape and pressure distribution can minimize friction drag by delaying the transition point, achieved by moving the widest point of the airfoil backward. Laminar airfoils maintain laminar flow longer, cutting friction drag to about half. Techniques like boundary layer suction can further affect transition and drag.

2.2.1 Stability

To analyze the stability of laminar flow, the motion is divided into the fundamental flow, which is to be assessed for stability, and an additional perturbation motion. Consider the fundamental flow as steady, with Cartesian velocity components denoted as U, V, W, and pressure P. This fundamental flow satisfies the Navier–Stokes equations or the boundary-layer equations. For the temporal disturbance, the respective quantities are u', v', w', and p'. Hence, the resulting flow encompasses the velocity and pressure

$$u = U + u', \quad v = V + v', \quad w = W + w', \tag{2.1}$$

$$p = P + p'. \tag{2.2}$$

Typically, it is presumed that the perturbation quantities are relatively small when compared to those of the fundamental flow. Analyzing the stability of a motion with such perturbations can be carried out by considering only those perturbations that align with the hydrodynamic equations of motion. The evolution of the disturbance over time is then followed using these differential equations, a technique known as *the method of small disturbances*.

A two-dimensional incompressible base flow, along with a two-dimensional disturbance, is assumed. Consequently, the flow described by Equation 2.1 and Equation 2.2 satisfies the two-dimensional Navier–Stokes equations. Furthermore, the base flow is chosen for simplicity, such that the U component is solely a function of y, specifically, $U = U(y)$, whereas the other velocity components are zero, $V = W = 0$. Nevertheless, for the pressure $P(x, y)$, it is essential to assume a dependency on x, as the

pressure gradient $\partial P/\partial x$ is responsible for sustaining the flow. Hence, the base flow is characterized by the form

$$U(y), \quad V = W = 0, \quad P(x, y). \tag{2.3}$$

Onto this basic flow, a two-dimensional perturbation is superimposed, which is also dependent on the time. For this, the velocity components and the pressure are

$$u'(x, y, t), \quad v'(x, y, t), \quad p'(x, y, t). \tag{2.4}$$

Therefore the resulting motion according to Equation 2.1 and Equation 2.2 is

$$u = U + u', \quad v = v', \quad w = 0, \quad p = P + p'. \tag{2.5}$$

The fundamental flow described in Equation 2.3 is considered a solution to the Navier–Stokes equations by assumption. Nonetheless, the subsequent motion depicted in Equation 2.5 must also adhere to the Navier–Stokes equations. The additional perturbation in Equation 2.4 is assumed to be ”small,” meaning that all quadratic perturbation terms are negligible when compared to the linear terms. The purpose of the stability analysis is to determine whether, for a specified basic flow, the disturbance decreases or increases over time. Accordingly, the basic flow is classified as stable or unstable, depending on the outcome.

Inserting Equation 2.5 into the Navier–Stokes equations of the two-dimensional incompressible unsteady flow (Equation 2.6), and ignoring all terms quadratic in the perturbation velocities results into Equation 2.7.

$$\begin{aligned}
\frac{\partial u}{\partial t} + u\frac{\partial u}{\partial x} + v\frac{\partial u}{\partial y} &= -\frac{1}{\rho}\frac{\partial p}{\partial x} + \nu\left(\frac{\partial^2 u}{\partial x^2} + \frac{\partial^2 u}{\partial y^2}\right), \\
\frac{\partial v}{\partial t} + u\frac{\partial v}{\partial x} + v\frac{\partial v}{\partial y} &= -\frac{1}{\rho}\frac{\partial p}{\partial y} + \nu\left(\frac{\partial^2 v}{\partial x^2} + \frac{\partial^2 v}{\partial y^2}\right), \\
\frac{\partial u}{\partial x} + \frac{\partial v}{\partial y} &= 0
\end{aligned} \tag{2.6}$$

$$\begin{aligned}
\frac{\partial u'}{\partial t} + U\frac{\partial u'}{\partial x} + v'\frac{dU}{dy} + \frac{1}{\rho}\frac{\partial p'}{\partial x} &= \nu\left(\frac{d^2 U}{dy^2} + \Delta u'\right), \\
\frac{\partial v'}{\partial t} + U\frac{\partial v'}{\partial x} + \frac{1}{\rho}\frac{\partial p'}{\partial y} &= \nu\Delta v', \\
\frac{\partial u'}{\partial x} + \frac{\partial v'}{\partial y} &= 0.
\end{aligned} \tag{2.7}$$

Here Δ is the operator $\partial^2/\partial x^2 + \partial^2/\partial y^2$.

If the basic flow must also itself satisfy the Navier–Stokes equations (in the case of the boundary layer, approximately) these equations simplify to

$$\begin{aligned}
\frac{\partial u'}{\partial t} + U\frac{\partial u'}{\partial x} + v'\frac{dU}{dy} + \frac{1}{\rho}\frac{\partial p'}{\partial x} &= \nu\Delta u', \\
\frac{\partial v'}{\partial t} + U\frac{\partial v'}{\partial x} + \frac{1}{\rho}\frac{\partial p'}{\partial y} &= \nu\Delta v', \\
\frac{\partial u'}{\partial x} + \frac{\partial v'}{\partial y} &= 0.
\end{aligned} \tag{2.8}$$

Three equations describe the perturbation quantities u', v', and p'. Boundary conditions require perturbation velocities u' and v' to vanish at walls, following the no-slip condition. Pressure p' is eliminated

from Equation 2.8, leaving two equations for u' and v' with continuity. Concerns about the parallel-flow assumption in Equation 2.3—neglecting variations in longitudinal velocity U with respect to x and normal component V—are alleviated, as these terms are negligible for boundary layer stability analysis.

2.2.2 The Orr-Sommerfeld equation

Consider the fundamental flow moving in the x direction with a velocity profile $U(y)$, upon which a disturbance is overlaid, consisting of basic partial perturbations or modes. Each of these modes represents a wave traveling in the x direction. For the (assumed) two-dimensional disturbance, a stream function $\psi(x, y, t)$ can be defined. This enables the integration of the continuity equation in Equation 2.8. The stream function for one mode within the disturbance employs the following trial solution:

$$\psi(x, y, t) = \varphi(y)\mathrm{e}^{\mathrm{i}(\alpha x - \beta t)}. \tag{2.9}$$

An arbitrary plane disturbance can be considered to be decomposed into such Fourier modes. Here α is real and $\lambda = 2\pi/\alpha$ is the wavelength of the perturbation. The quantity β is complex

$$\beta = \beta_\mathrm{r} + \mathrm{i}\beta_\mathrm{i}, \tag{2.10}$$

β_r represents the frequency of the mode, while β_i, the amplification factor, indicates if the wave experiences growth or diminishes. When $\beta_\mathrm{i} < 0$, the wave is attenuated, signifying a stable laminar flow, whereas $\beta_\mathrm{i} > 0$ signals the presence of instabilities. Besides α and β, it is beneficial to also define the combined quantity

$$c = \frac{\beta}{\alpha} = c_\mathrm{r} + \mathrm{i}c_\mathrm{i}\ . \tag{2.11}$$

Here, c_r represents the phase velocity of the wave along the x direction, whereas c_i determines if the wave will amplify or diminish, contingent upon whether c_i is positive or negative. The disturbance's amplitude function $\varphi(y)$ is specified to rely solely on y, given that the primary flow is solely a function of y. This equation provides the components of the perturbation velocity as

$$u' = \frac{\partial \psi}{\partial y} = \varphi'(y)\mathrm{e}^{\mathrm{i}(\alpha x - \beta t)}, \tag{2.12}$$

$$v' = -\frac{\partial \psi}{\partial x} = -\mathrm{i}\alpha\varphi(y)\mathrm{e}^{\mathrm{i}(\alpha x - \beta t)}. \tag{2.13}$$

Inserting these in the two momentum equations in Equation 2.8, and eliminating the pressure, the following fourth order ordinary differential equation is found for the amplitude function $\varphi(y)$:

$$\boxed{(U - c)(\varphi'' - \alpha^2\varphi) - U''\varphi = -\frac{\mathrm{i}}{\alpha\,\mathrm{Re}}(\varphi'''' - 2\alpha^2\varphi'' + \alpha^4\varphi).} \tag{2.14}$$

This differential equation with perturbations serves as the foundation for the stability theory of laminar flow. In Equation 2.14, all variables have been made dimensionless by relating lengths to the selected reference length δ (the boundary-layer thickness) and velocities to the maximum velocity of the basic flow U_e (i.e. to the velocity at the outer edge of the boundary layer). The dash means differentiation with respect to the dimensionless coordinate y/δ, while

$$Re = \frac{U_e\delta}{\nu} \tag{2.15}$$

is the characteristic Reynolds number for the given mean flow. The expressions on the left side of Equation 2.14 account for the inertial terms, whereas those on the right side originate from the frictional

terms of the equations of motion. The boundary conditions for a boundary-layer flow where both velocity components or the disturbance vanish at the wall ($y = 0$) and at large distances from the wall (outer flow) are:

$$\begin{aligned} y = 0: &\quad u' = v' = 0, \quad \varphi = 0, \quad \varphi' = 0, \\ y = \infty: &\quad u' = v' = 0, \quad \varphi = 0, \quad \varphi' = 0. \end{aligned} \tag{2.16}$$

As experimental findings suggest that the stability threshold $c_i = 0$ is anticipated at high Reynolds numbers, it appears logical to simplify the overall perturbation equation (Equation 2.14) by disregarding the right-hand side friction terms, since they are scaled down by the small factor $1/Re$ in relation to the left-hand side inertial terms. This leads to the derivation of the inviscid perturbation differential equation:

$$(U - c)(\varphi'' - \alpha^2\varphi) - U''\varphi = 0. \tag{2.17}$$

As this equation is second order, just two of the four boundary conditions (Equation 2.16) can be met. For inviscid flow, these conditions involve the normal component of the perturbation velocity disappearing at one wall and at a considerable distance from the wall in boundary-layer flow. They read

$$y = 0: \quad \varphi = 0, \qquad y \to \infty: \quad \varphi = 0. \tag{2.18}$$

2.2.3 The eigenvalue problem

The stability analysis of a laminar flow is now an eigenvalue problem of the perturbation differential equation Equation 2.14 with the boundary conditions Equation 2.16. For a given basic flow $U(y)$, Equation 2.14 contains four parameters, namely Re, α, c_r and c_i. Of these, the Reynolds number of the basic flow is likewise specified, and in addition the wavelength $\lambda = 2\pi/\alpha$ of the perturbation can be taken as given. Therefore, for every pair α, Re, Equation 2.14 with boundary conditions Equation 2.14 yields an eigenfunction $\varphi(y)$ and a complex eigenvalue $c = c_\mathrm{r} + \mathrm{i}\, c_\mathrm{i}$. Here c_r is the phase velocity of the given perturbation, while the sign of c_i determines the stability ($c_\mathrm{i} < 0$) or instability ($c_\mathrm{i} > 0$) of the basic flow. The limiting case $c_\mathrm{i} = 0$ gives neutral (indifferent) disturbances. These circumstances describe the temporal amplification or decay of the disturbance.

With the assumption that perturbations evolve over time, the outcomes of stability analysis for a specific laminar flow $U(y)$ can be depicted by assigning a pair of values c_r and c_i to each coordinate in the α–Re plane. Specifically, the line where $c_\mathrm{i} = 0$ serves as a boundary distinguishing stable solutions from unstable ones. This boundary is known as the *curve of neutral stability* (Figure 2.5). The point of particular interest on this curve is where the Reynolds number reaches its minimum value, specifically where the curve of neutral stability is tangent to the α-axis. This point defines the Reynolds number below which all disturbance modes are suppressed, whereas above it, some modes begin to grow. This minimum value of the Reynolds number on the curve of neutral stability is known as the theoretical indifference Reynolds number or the limit of stability of the laminar flow under investigation.

According to the experimental results on the laminar–turbulent transition discussed above, it is expected that at low Reynolds numbers—where the flow remains laminar—only stable disturbances exist across all wavelengths. On the other hand, at high Reynolds numbers, where the flow turns turbulent, unstable perturbations occur for at least some wavelengths. Nevertheless, it's important to acknowledge that the theoretically calculated indifference Reynolds number through linear stability analysis won't necessarily match the critical Reynolds number seen in experiments that signify the laminar–turbulent transition.

When a parabolic base flow (Poiseuille flow) is taken into consideration, there is one mode that first becomes unstable (for nonzero values of α (Equation 2.9). According to Rayleigh's inflection point criterion, the Poiseuille profile is stable as $Re \to \infty$, so one must conclude that viscosity is in this case destabilizing. This unstable eigenmode is called a Tollmien-Schlichting wave and is the first evidence that the Orr-Sommerfeld equation has unstable disturbances for flows without inflection points [18].

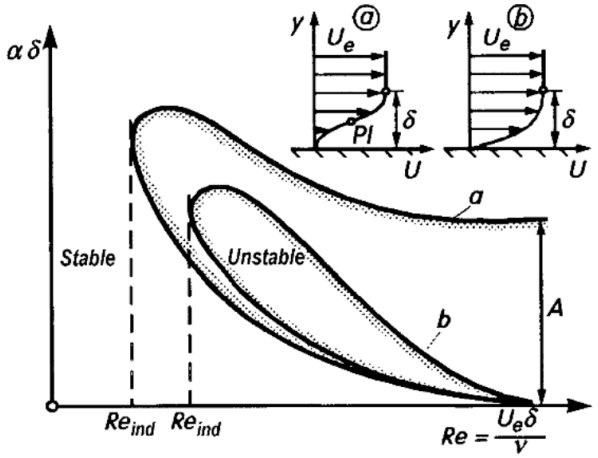

Figure 2.5: Curves of neutral stability of a plane boundary layer for two-dimensional incompressible perturbations: (a) "Inviscid" instability — for type (a) velocity profiles with point of inflection PI, the curve of neutral stability is of type (a). The asymptotes of this curve for $\mathrm{Re} \to \infty$ are obtained from the inviscid perturbation differential equation (Equation 2.17). (b) "Viscous" instability — for type (b) velocity profiles without point of inflection, the curve of neutral stability is of type (b). A: inviscid instability. [2]

2.3 Flow control methods

A wide variety of different types of flow control strategies — active, passive, open-loop, closed-loop, etc. — have been developed and implemented over the years, and some are quite successful in achieving certain control objectives. Several recent and comprehensive surveys of this rapidly growing field are available [5]. During the early 1990s, experts in fluid dynamics observed that numerous new ideas in hydrodynamic stability theory were already present within linear systems theory.

2.3.1 Review of previous work on active flow control

Jovanovic & Bamieh [19] investigated the linearized Navier–Stokes equations around parallel channel flows using an input–output framework to analyze how spatially and temporally varying three-dimensional body forces influence the velocity components. Through frequency-domain analysis he identified dominant amplification mechanisms associated with subcritical transition phenomena, such as Tollmien–Schlichting waves, oblique waves, and streamwise vortices.

Schmid emphasizes that the non-normality of the linearized Navier–Stokes operator in wall-bounded shear flows limits the effectiveness of classical eigenvalue analysis, which primarily captures the long-term behavior of disturbances but often overlooks crucial short-time dynamics [20]. To address this, he highlights the use of tools such as the matrix exponential, resolvent operators, and solutions to the Lyapunov and covariance equations, which allow for a comprehensive analysis of both deterministic and stochastic perturbations.

In Joshi's et al. work on the stabilization of plane Poiseuille flow [21], the authors develop feedback controllers based on state-space models derived via a Galerkin spectral method, using Fourier modes in the streamwise direction and Chebyshev polynomials in the wall-normal direction. This approach yields a block-diagonal system matrix due to the decoupling of dynamics by wavenumber, enabling a clear delineation between modeled and unmodeled dynamics. Such structure facilitated the use of distributed control strategies, especially by rendering certain wavenumbers effectively uncontrollable.The study highlights how different sensor placements can lead to either minimum-phase or non-minimum-phase behavior, with significant implications for controller design. Stabilization was achieved using simple feedback mechanisms, including integral compensator controllers, which demonstrated robust performance across a range of Reynolds numbers. However, the authors caution that transient growth in the linear response - even in controlled systems - can potentially trigger nonlinear effects not captured by the model. Nevertheless, the proposed controllers were shown to suppress two-dimensional finite-amplitude disturbances and stabilize secondary three-dimensional instabilities, underscoring the potential of linear feedback control in managing transitional flows.

The study of Bewley and Liu [22] demonstrates the superior performance of modern controllers over

classical proportional control, especially in cases with non-orthogonal eigenmodes. Using transfer function norms and transient energy growth as key performance metrics, the analysis reveals that root locus techniques alone are insufficient to fully capture the behavior of non-normal systems. A novel scaling framework for H_∞ estimation enables independent tuning of three scalar parameters $\{\gamma, \mathbf{z}, t\}$ to optimize performance in large MIMO systems, maintaining the duality between estimation and control. The flow is shown to be stabilizable (but not fully controllable) via wall-normal actuation and detectable (but not observable) using wall skin-friction measurements. This methodology offers a flexible and efficient means of achieving desirable trade-offs among disturbance rejection, feedback minimization, and robustness in closed-loop flow control systems.

Building on state-feedback control strategies and incorporating some improved estimation techniques proposed, effective control of viscous instabilities, transient energy growth, and inflectional instabilities in spatially developing boundary layers has been achieved using only wall-based measurements by Chevalier et al. [23]. A central contribution to the enhanced estimator performance is the development of a physically informed stochastic disturbance model. This model uses a spatial correlation structure weighted more heavily inside the boundary layer and an amplitude distribution in wavenumber space tailored to the dominant flow structures, resulting in well-resolved estimation gains for wall-based measurements, including streamwise and spanwise skin friction as well as wall pressure. Importantly, the state estimate converges upstream of this transient, ensuring that accurate information is available above the actuation region in time for effective control, thereby improving the efficiency and responsiveness of the compensator.

The study done by Monokrousos et al. [24] investigates bypass transition in boundary-layer flows subjected to high levels of free-stream turbulence, emphasizing the growth and secondary instability of streamwise streaks. Large-eddy simulations (LES) using the ADM-RT subgrid-scale model are validated and shown to effectively capture the transition process while reducing computational cost compared to direct numerical simulation (DNS). A linear feedback control strategy, based on wall-shear stress measurements and designed through linear stability theory, is employed to delay transition. The control reduces streak energy and delays turbulence onset, leading to an estimated drag reduction of 5–10%. However, its effectiveness is limited downstream due to the rapid recovery of streaks. The study also identifies limitations in flow field estimation from wall data alone and suggests future improvements via model reduction or data-driven sensor-actuator mapping.

Active control for transition delay has has been advanced from a more practical approach, utilizing system identification and active wave-cancellation techniques. The majority of research, though not entirely, relies on experimental studies, which, due to feasibility issues, often prioritize engineering solutions and sometimes ad hoc techniques. An early example of this method is seen in Milling's study [25], where TS waves were controlled by implementing wave cancellation control; this involves generating perturbations with opposite phases to neutralize the propagating waves.

Although in the majority of experimental active control most controllers are developed directly in the experimental setting on a trial-and-error basis, there are some exceptions, like the work of Goldin et al. [26]. There, the use of membrane-based actuators demonstrated effective damping of natural multi-frequency Tollmien–Schlichting (TS) waves, achieving promising results. When coupled with an ODE-based wall model, the system mimics a compliant wall and achieves damping performance comparable to direct actuation.

2.3.2 A linear systems approach to flow control

In this section the essential ingredients of linear model–based systems and control theory as it relates to both transitional and turbulent fluid mechanical systems are presented and discussed.

An increasingly promising method for managing flow involves using linear systems and control theory [4]. This technique involves linearizing the fundamental equations governing fluid motion around a stable or average flow, enabling the formulation of feedback control strategies that systematically manipulate the flow via actuators and sensors. Despite turbulence being nonlinear and occurring across multiple scales, linear models frequently encapsulate critical dynamics for successful control. This model-based approach allows for the application of robust tools like optimal control, estimation theory, and model reduction, thereby forming a strong base for progressing both theoretical insights and

practical flow control technologies.

One fundamental case in flow control is the feedback problem, where the aim is to coordinate actuator inputs based on sensor outputs to achieve a specific outcome. A primary example in this context is channel flow, which uses skin friction and pressure sensors distributed along the walls to obtain system measurements, while zero-net blowing or suction is applied in a continuous manner along the walls for actuation. Despite being straightforward to analyze, this setup is somewhat idealized; various modifications are necessary to align it with real-world scenarios. This includes the consideration of spatially developing boundary layers, the specific positioning of sensors and actuators, their exact sensitivities, effects, and different sources of system uncertainty. Many of these extensions are well underway. Early investigations in the present vein include, among others, Joshi et al. [21], and Bewley and Liu [22].

Linear systems theory provides a uniquely effective tool for optimization and control. Any smooth problem is easily linearized. In partial differential equation (PDE) systems, linearization of the governing equations can be performed either algebraically by hand derivation and coding, or automatically via one of three approaches:

1. Utilizing an automatic differentiation tool for a nonlinear simulation code that implements the governing equations. It's worth noting that certain tools are also capable of generating the adjoint equation, which is central to a related optimization problem.
2. Carrying out a perturbed nonlinear simulation, then subtracting it from an unperturbed nonlinear simulation, followed by dividing by the perturbation's magnitude (using a finite difference method).
3. By changing real types to complex types throughout an entire nonlinear simulation code, then perturbing the optimization variables a small amount in the imaginary direction; the resulting linearized perturbation to the system is then evident in the imaginary part of the complex result [27]

The main difference between the iterative (adjoint-based) and direct (Riccati-based) methods lies in the state chosen for linearization. In the iterative approach, linearization occurs around an actual system trajectory. It then ascertains the optimal direction to adjust the optimization variables through this linearized analysis, modifies the variables to maximize benefit, and repeats this process. At each step, a new linearization of the governing equations is performed based on the complete nonlinear system trajectory using the current optimization variable values. Through a sequence of such linear analyses, this method aims to optimize the entire nonlinear problem, although the (local) optimal point so found is not guaranteed to be the globally optimal solution.

Conversely, the direct method involves performing a single linearization around a typical mean flow condition, which may also act as a solution to the governing equations. By simplifying the problem in this manner, this method directly reaches the singular optimal point of the simplified optimization problem being addressed. Ultimately, both the iterative (adjoint-based) and direct (Riccati-based) methods are intrinsically linked, relying fundamentally on the principles of linearization and optimization.

The research question of this thesis is : "Is the adjoint method an efficient computational tool for large scale control-flow problems?"

3

Numerical methodology

3.1 Mathematical structure of the Kuramoto–Sivashinsky equation

The KS (Kuramoto-Sivashinsky) equation was initially formulated to characterize the oscillations of the flame front in laminar flames [6], [7]. In its spatially periodic variant, this model displays spatiotemporal chaotic dynamics, which exhibit certain resemblances to turbulence [28]. The typical KS equation is expressed as

$$\frac{\partial \tilde{v}}{\partial \tilde{t}} + \tilde{v}\frac{\partial \tilde{v}}{\partial \tilde{x}} = -\eta\frac{\partial^2 \tilde{v}}{\partial \tilde{x}^2} - \mu\frac{\partial^4 \tilde{v}}{\partial \tilde{x}^4} \tag{3.1}$$

where $\tilde{t}$ is the time, $\tilde{x} \in [0, \tilde{L})$ the spacial coordinate and $\tilde{v} = \tilde{v}(\tilde{x}, \tilde{t})$ the velocity. The terms in this equation from left to right are the typical time derivative, the nonlinear convection term and two viscosity terms on the right hand sight. These two terms are associated with the production ad dissipation of the energy at different spatial scales. Specifically, the second order derivative corresponds to the production of the energy via the parameter η called "antiviscosity" while the dissipation of the energy comes from the fourth order derivative and is affected by the parameter μ that is called "hyperviscocity".

In order to use the equation in a parametrized form, it can be rearranged with a help of a Reynolds-number-like coefficients. The non-dimensionality is introduced via the reference length $\tilde{l}$ and the reference velocity $\tilde{V}$, which define the non-dimensional position x, velocity v and time t

$$x = \frac{\tilde{x}}{l}, \quad v = \frac{\tilde{v}}{\tilde{V}}, \quad t = \frac{\tilde{t} \cdot \tilde{V}}{l} \tag{3.2}$$

Applying the transformation to Equation 3.1, the dimensionless form of the KS equation is obtained as

$$\frac{\partial v}{\partial t} + v\frac{\partial v}{\partial x} = -\frac{1}{\mathcal{R}}\left(\mathcal{P}\frac{\partial^2 v}{\partial x^2} + \frac{\partial^4 v}{\partial x^4}\right) \tag{3.3}$$

where $x \in [0, L)$. The coefficients $\mathcal{R}$ and $\mathcal{P}$ are defined as

$$\mathcal{R} = \frac{\tilde{V}\tilde{l}^3}{\mu}, \qquad \mathcal{P} = \frac{\eta}{\mu}\tilde{l}^2 \tag{3.4}$$

where $\mathcal{R}$ acts as the Reynolds number while $\mathcal{P}$ regulates the balance between energy production and dissipation.

One basic assumption behind this mathematical formulation is that the system is sufficiently close to a steady state solution $V(x)$. Having that as a basis, the dynamics of perturbations can be represented

by the linearized KS equation. Although for certain parameters the steady solution can be stable, an external perturbation may be amplified by an order-of-magnitude before it dies out. This fact introduces the need of non-periodic boundary conditions in the streamwise direction as they are introduced later. At this point, the perturbation $v'(x)$ can be introduced

$$v(x,t) = V + \varepsilon v'(x,t) \tag{3.5}$$

where $\varepsilon << 1$. The linearized KS equation is a result of inserting this formulation into Equation 3.3 and neglecting the terms of order ε^2 and higher.

$$\frac{\partial v'}{\partial t} = -V\frac{\partial v'}{\partial x} - \frac{1}{\mathcal{R}}\left(\mathcal{P}\frac{\partial^2 v'}{\partial x^2} + \frac{\partial^4 v'}{\partial x^4}\right) \tag{3.6}$$

If the non-linear effect of the equation needs to be studied, an additional term that was initially neglected due the assumption that $\varepsilon << 1$ needs to be introduced. This term is $-\varepsilon v' \frac{\partial v'}{\partial x}$ and is dependent on the magnitude of ε. The higher the value of ε the more evident the non-linear effects become. This will be analyzed further in chapter 4

$$\frac{\partial v'}{\partial t} = -V\frac{\partial v'}{\partial x} - \frac{1}{\mathcal{R}}\left(\mathcal{P}\frac{\partial^2 v'}{\partial x^2} + \frac{\partial^4 v'}{\partial x^4}\right) - \varepsilon v'\frac{\partial v'}{\partial x} \tag{3.7}$$

The convective and amplifying characteristics of this non-normal system render it an effective representation of the 2D Blasius boundary layer flow. In order to analyze the stability of Equation 3.6, a traveling wave-like solution is assumed

$$v' = \hat{v}e^{i(\alpha x - \omega t)} \tag{3.8}$$

where $a \in \mathbb{R}$ and $\omega = \omega_r + \omega_i \in \mathbb{C}$. If Equation 3.8 in Equation 3.6, a dispersion relation between the spatial wave-number a and the temporal frequency ω is obtained

$$\omega = V\alpha + \mathrm{i}\left(\frac{\mathcal{P}}{\mathcal{R}}\alpha^2 - \frac{1}{\mathcal{R}}\alpha^4\right) \tag{3.9}$$

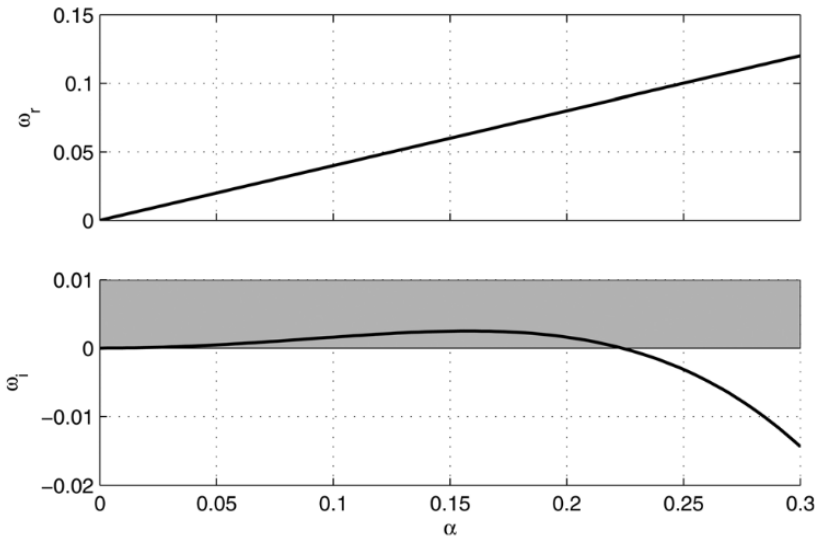

Figure 3.1: The real and imaginary parts of the frequency ω. The gray area describes positive values of ω_i which means unstable waves.

The parameters $\mathcal{R} = 0.25$, $\mathcal{P} = 0.05$, and $V = 0.4$ are selected to simulate the Blasius boundary layer at $Re_{\delta^*} = 1000$. The imaginary component of the frequency ω_i represents the exponential rate of temporal growth for a wave with wave-number a. According to Equation 3.9, the term involving a^2 (linked with the production parameter $\mathcal{P}$) contributes positively to ω_i, whereas the a^4 term (associated with the dissipation parameter $\mathcal{R}$) acts as a stabilizing influence. The interplay of these terms dictates the stability of the wave under consideration. From Figure 3.1, it can be seen that for certain wave-number ranges a, $\omega_i > 0$, indicating the wave is unstable. The real part ω_r defines the wave's phase speed in the x direction

$$c \triangleq \frac{\omega_r}{\alpha} = V \tag{3.10}$$

The main goal of this mathematical framework is to model the amplification of a propagating wave-packet near a stable steady solution, like the case of boundary layer flow. Thus, the outflow boundary condition on the right side of the domain needs to be

$$\left.\frac{\partial^3 v'}{\partial x^3}\right|_{x=L} = 0, \quad \left.\frac{\partial v'}{\partial x}\right|_{x=L} = 0 \tag{3.11}$$

while on the left side of the domain, at the inlet, an unperturbed boundary condition is enforced

$$v'|_{x=0} = 0, \quad \left.\frac{\partial v'}{\partial x}\right|_{x=0} = 0 \tag{3.12}$$

If an outflow boundary condition is imposed, an initial localized disturbance introduced in the upstream area of the domain moves downstream, experiencing exponential growth in amplitude until it exits the domain. All convectively unstable flows have this is characteristic.

3.2 Defining inputs and outputs

Following the description of the linear system's dynamics, a systematic examination of the inputs (actuators/disturbances) and sensor outputs is conducted. The linearized KS equation (Equation 3.6) is taken into account, (this applies to the non-linear equation as well)

$$\frac{\partial v'}{\partial t} = -V\frac{\partial v'}{\partial x} - \frac{1}{\mathcal{R}}\left(\mathcal{P}\frac{\partial^2 v'}{\partial x^2} + \frac{\partial^4 v'}{\partial x^4}\right) + f'(x,t) \tag{3.13}$$

where the forcing term $f'(x,t)$ now appears on the right hand side. This term is decomposed into two parts

$$f'(x,t) = b_d(x)d(t) + b_u(x)u(t) \tag{3.14}$$

The temporal signal of the incoming external disturbance and of the actuator are denoted by $d(t)$ and $u(t)$, respectively, while the corresponding spatial distribution is described by $b_d(x)$ and $b_u(x)$. The time-independent spatial distribution of the inputs is described by the Gaussian function

$$g(x;\hat{x},\sigma) = \frac{1}{\sigma}\exp\left[-\left(\frac{x-\hat{x}}{\sigma}\right)^2\right] \tag{3.15}$$

The scalar parameter σ determines the width of the Gaussian distribution, whereas $\hat{x}$ determines the center of the Gaussian. The two forcing distributions in Equation 3.14 are

$$b_d(x) = g(x;\hat{x}_d,\sigma_d),\ b_u(x) = g(x;\hat{x}_u,\sigma_u) \tag{3.16}$$

The position of the disturbance d is in the beginning of the domain at $x_d = 35$, while the actuator u is placed in the middle of the domain at $x_u = 400$ (Figure 3.2). The particular shape $b_d(x)$ of the disturbance d is part of the modeling process. The introduction of the upstream disturbance using a localized and well defined shape $b_d(x)$ is a model. In practical cases, due to the receptivity processes, there is no knowledge around the distribution and the appearance of the incoming disturbance beforehand, and thus they are difficult to predict using, for instance, a low-order model.

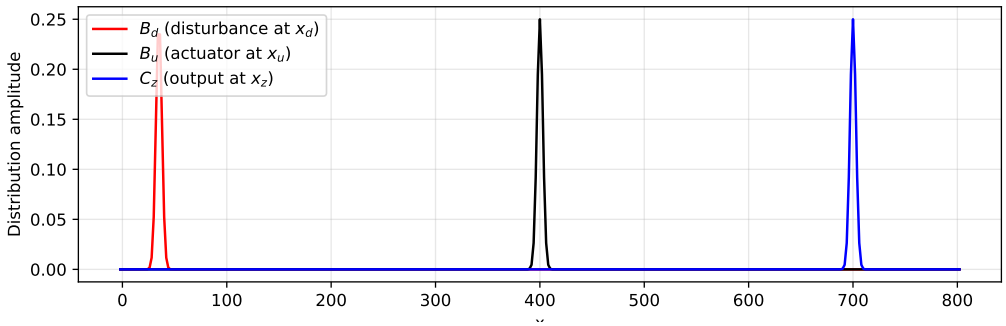

Figure 3.2: Spatial support functions used for the inputs and outputs along the streamwise direction. All standard deviation parameters are the same $\sigma_d = \sigma_u = \sigma_z = 4$

A comparable problem might occur with the actuator model $b_u(x)$, where the forcing distribution could also vary over time.

For instance, the spatial force exerted by a plasma actuator within a flow is influenced by the input voltage, such as the amplitude $u(t)$ [29]. If Equation 3.15 is used as the integration weight, the output of the system is defined as

$$z(t) = \int_0^L c_z(x) v'(x,t)\, dx \tag{3.17}$$

where L is the length of the domain defined earlier and

$$c_z(x) = g(x; \hat{x}_z, \sigma_z) \tag{3.18}$$

The output $z(t)$, located far downstream, represents the objective of the controller: assuming that the flow has been already modified due to the action of the controller, this controlled output is the quantity that is desired to be kept as small as possible.

First the linear, then the non-linear We discretize the spatial part of Equation 3.13 by a finite-difference scheme. The solution is approximated by

$$v_i'(t) = v'(x_i, t), \quad i = 1, 2, \ldots, n_\mathrm{v} \tag{3.19}$$

defined on the equispaced nodes $x_i = iL/n_v$, where $n_v = 400$. The spatial derivatives are approximated by a finite-difference (FD) scheme based on five-point stencils. Boundary conditions in Equation 3.12, Equation 3.11 are imposed using four ghost nodes $i = -1, 0$ and $i = n_v + 1, n_v + 2$. The resulting finite-dimensional state-space system is

$$\dot{\mathbf{v}}(t) = \mathbf{A}\mathbf{v}(t) + \mathbf{B}_d d(t) + \mathbf{B}_u u(t) \tag{3.20}$$

$$\dot{z}(t) = \mathbf{C}_z \mathbf{v}(t) \tag{3.21}$$

where $\mathbf{v} \in \mathbb{R}^{n_v}$ represents the nodal values v_i' . The output matrix $\mathbf{C_z}$ approximates the integral in Equation 3.17 via the trapezoidal rule, while the input matrices $\mathbf{B}_d$ and $\mathbf{B}_u$ are given by the evaluation of Equation 3.16 at the nodes. Some of the control algorithms that we will describe are preferably formulated in a time-discrete setting. The time-discrete variable corresponding to $a(t)$ is

$$a(k) = a(k\Delta t), \quad k = 1, 2, \dots \tag{3.22}$$

where Δt is the sampling time. Accordingly, the time-discrete state-space system is defined as

$$\begin{aligned} \mathbf{v}(k+1) &= \widetilde{\mathbf{A}}\mathbf{v}(k) + \widetilde{\mathbf{B}}_d d(k) + \widetilde{\mathbf{B}}_u u(k) \\ z(k) &= \widetilde{\mathbf{C}}_z \mathbf{v}(k) \end{aligned}$$

where $\widetilde{\mathbf{A}} = \exp(\mathbf{A}\Delta t)$, $\widetilde{\mathbf{B}} = \Delta t \mathbf{B}$, and $\widetilde{\mathbf{C}} = \mathbf{C}$.

3.3 Model based control

In this section, the full knowledge of the state $v(t)$ is assumed for the computation of the control signal $u(t)$. This signal is fed back into the system in order to minimize the energy of the output $z(t)$. For linear systems, it is possible to identify a feedback gain $\mathbf{K}(t)$, relating the control signal to the state, i.e.,

$$u(t) = \mathbf{K}(t)\mathbf{v}(t) \tag{3.23}$$

The aim of the section is to compare and link the classical LQR problem [8] to the more general adjoint approach. In the former approach, one assumes an infinite time horizon $(t \to \infty)$, allowing the computation of the feedback gain by solving a Riccati equation. In the latter approach, the optimization is performed with a final time T. Note that the framework introduced in this section makes use of a system's model.

The aim of the controller is to compute a control signal $u(t)$ in order to minimize the norm of the fictitious output

$$z'(t) = \begin{bmatrix} z(t) \\ u(t) \end{bmatrix} = \begin{bmatrix} \mathbf{C}_z \\ \mathbf{0} \end{bmatrix} \mathbf{v}(t) + \begin{bmatrix} 0 \\ 1 \end{bmatrix} u(t) \tag{3.24}$$

where now the control signal is also included. A cost function of the system can be defined as

$$\mathcal{L}(\mathbf{v}(u), u) = \frac{1}{2} \int_0^T \begin{bmatrix} z \\ u \end{bmatrix}^H \begin{bmatrix} w_z & 0 \\ 0 & w_u \end{bmatrix} \begin{bmatrix} z \\ u \end{bmatrix} dt \tag{3.25}$$

This cost function is quadratic and includes the constant matrices $w_z > 0$ and $w_u > 0$. The matrix w_z is used to normalize the cost output, specially when multiple $z(t)$ are used, while the weight w_u determines the amount of penalty on control effort. In this particular case, the values that are used are $w_z = 1, w_u = 1$. Using Equation 3.24, Equation 3.25 is rewritten as

$$\begin{aligned} \mathcal{L}(\mathbf{v}(u), u) &= \frac{1}{2} \int_0^T \left(\mathbf{v}^H \left(\mathbf{C}_z^H w_z \mathbf{C}_z \right) \mathbf{v} + u^H w_u u \right) dt \\ &= \frac{1}{2} \int_0^T \left(\mathbf{v}^H \mathbf{W}_\mathbf{v} \mathbf{v} + u^H w_u u \right) dt \end{aligned} \tag{3.26}$$

where $\mathbf{W_v} = \mathbf{C}_z^H w_z \mathbf{C}_z$. The sensor $\mathbf{C}_z$ is placed far downstream in the domain, so the energy is minimized in that localized region. The final goal of this procedure is a control signal $u(t)$ that minimizes the cost function $\mathcal{L}(\mathbf{v}(u), u)$ in some time interval $t \in [0, T]$ subject to the dynamic constraint

$$\dot{\mathbf{v}}(t) = \mathbf{A}\mathbf{v}(t) + \mathbf{B}_u u(t) \tag{3.27}$$

It is important to highlight that the disturbance $d(t)$ is excluded from the resolution of the optimal control problem. In a variational approach, one defines a Lagrangian

$$\begin{aligned}\mathcal{L}(\mathbf{v}(u), u) = \frac{1}{2}\int_0^T \left(\mathbf{v}^H \mathbf{W}_v \mathbf{v} + u^H w_u u\right) dt \\ + \int_0^T \mathbf{p}^H \left(\dot{\mathbf{v}} - \mathbf{A}\mathbf{v} - \mathbf{B}_u u\right) dt\end{aligned} \tag{3.28}$$

where the term $p(t)$ acts as a Lagrangian multiplier (also called the adjoint state). The expression in the last term is obtained via integration by parts. Instead of minimizing L with a constraint (Equation 3.27) one may minimize $\tilde{\mathcal{L}}$ without any constraints. The dynamics of the adjoint state $p(t)$ is obtained by requiring $\frac{\partial \widetilde{\mathcal{L}}}{\partial \mathbf{v}} = 0$, which leads to

$$\begin{aligned}-\dot{\mathbf{p}}(t) &= \mathbf{A}^H \mathbf{p}(t) + \mathbf{W}_\mathbf{v} \mathbf{v}(t) \\ \mathbf{0} &= \mathbf{p}(T)\end{aligned} \tag{3.29}$$

The adjoint field $p(t)$ is computed by marching backward in time this equation, from $t = T$ to $t = 0$. The optimality condition is obtained by the gradient

$$\frac{\partial \widetilde{\mathcal{L}}}{\partial u} = \mathbf{B}_u^H \mathbf{p} + w_u u \tag{3.30}$$

The resulting equations' system can be solved iteratively as follows:

1. The state $v(t)$ is computed by marching forward in time Equation 3.27 in $t \in [0, T]$. At the first iteration step, $k = 1$, an initial guess is taken for the control signal $u(t)$.
2. The adjoint state $p(t)$ is evaluated marching Equation 3.29 backward in time, from $t = T$ to $t = 0$. The initial condition $p(T)$ is taken to be zero.
3. Once the adjoint state $p(t)$ is available, it is possible to compute the gradient via Equation 3.30 and apply it for the update of the control signal using a gradient-based method; one may, for example, apply directly the negative gradient $\Delta u_k = -\frac{\partial \widetilde{\mathcal{L}}_k}{\partial u}$, such that the update of the control signal at each iteration is given by

$$u_{k+1} = u_k + \mu_k \Delta u_k \tag{3.31}$$

The scalar-valued parameter μ_k is the step-length for the optimization, also known as the learning rate. The iteration stops when the difference of the cost function $\mathcal{L}$ estimated at two successive iteration steps is below a certain tolerance or the gradient value $\frac{\partial \widetilde{\mathcal{L}}}{\partial u} \to 0$.

The mathematical framework outlined in the previous section is rather general and it can be applied for the computation of the control signal $u(t)$ also when nonlinear systems are considered. However, a drawback of the procedure is the necessity of running an optimization on-line, next to the main flow simulation/experiment. When a linear time-invariant system is considered, a classic way to proceed is to directly use the optimal condition Equation 3.30 in order to identify the optimal control signal $u(t)$

$$u(t) = -w_u^{-1}\mathbf{B}_u^H\mathbf{p}(t) \tag{3.32}$$

The computed control signal $u(t)$ is optimal as it minimizes the cost function $\mathcal{L}(\mathbf{v}(u), u)$ previously defined. Assuming a linear relation between the adjoint state and the direct state, $\mathbf{p}(t) = \mathbf{X}(t)\mathbf{v}(t)$, the feedback gain is given by

$$\mathbf{K}(t) = -\mathbf{R}_u^{-1}\mathbf{B}_u^H\mathbf{X}(t) \tag{3.33}$$

It can be shown that the matrix $\mathbf{X}(t)$ is the solution of a differential Riccati equation [8]. When $\mathbf{A}$ is stable, $\mathbf{X}(t)$ reaches a steady state as $T \to \infty$, which is a solution of the algebraic Riccati equation

$$\mathbf{0} = \mathbf{A}^H\mathbf{X} + \mathbf{X}\mathbf{A} - \mathbf{X}\mathbf{B}_u\mathbf{R}_u^{-1}\mathbf{B}_u^H\mathbf{X} + \mathbf{Q} \tag{3.34}$$

A key benefit of this method is that $\mathbf{X}$ remains constant, and needs to be computed just once. The spatial arrangement of the control gain $\mathbf{K}$ is depicted in Figure 3.3 for the KS system discussed previously, where the actuator is positioned at $x = 400$ and the target output at $x = 700$. As evident from Figure 3.3, the gain is a concise construct between elements $\mathbf{B}_u$ and $\mathbf{C}_z$. Notably, the control gain is unaffected by the form of the external disturbance $\mathbf{B}_d$.

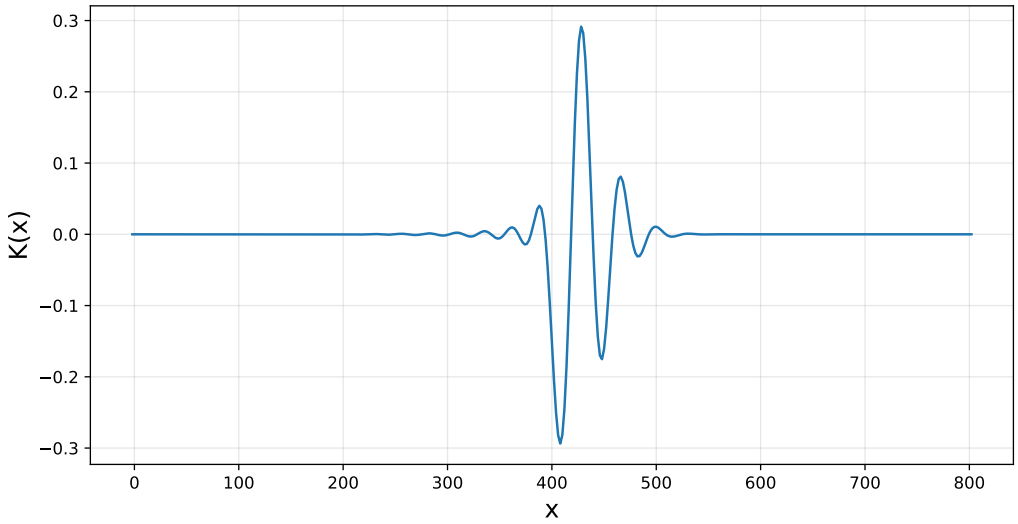

Figure 3.3: Control gain K computed using the LQR technique

3.4 Spatio-temporal discretization

Finite Difference (FD) schemes are employed to approximate the spatial derivatives in Equation 3.13. Specifically, a centered scheme utilizing stencils with five nodes is applied for both the second and fourth-order derivatives, whereas a one-node-backward scheme is implemented for the first-order derivative. This latter approach is necessitated by the convective characteristics of the system; using a decentered scheme helps mitigate undesired numerical oscillations in the solution approximation. The grid is uniformly spaced as $x_i = iL/n_v$, where $i = 1, 2, \ldots, n_\mathrm{v}$. With the FD scheme defined, the time progression at each internal node resolves into an ordinary differential equation (ODE) solution.

$$\frac{dv_i'(t)}{dt} = -V\sum_{j=-3}^{1} d_{1,j}^b\, v_{i+j}'(t) - \frac{\mathcal{P}}{\mathcal{R}}\sum_{l=-2}^{2} d_{2,l}^c\, v_{i+l}'(t) - \frac{1}{\mathcal{R}}\sum_{l=-2}^{2} d_{4,l}^c\, v_{i+l}'(t) + b_d(x_i)\, d(t) + b_u(x_i)\, u(t) \tag{3.35}$$

where $v'_i = v'(x_i, t)$ for $i = 1, 2, \ldots, n_\mathrm{v}$. The outflow boundary conditions in Equation 3.11 on the right boundary of the domain lead to the linear system of equations

$$\left.\frac{\partial v'}{\partial x}\right|_{x=L} = 0 \quad \Rightarrow \quad \sum_{j=-3}^{1} d^b_{1,j}\, v'_{n_q+j}(t) = 0 \tag{3.36}$$

$$\left.\frac{\partial^3 v'}{\partial x^3}\right|_{x=L} = 0 \quad \Rightarrow \quad \sum_{j=-2}^{2} d^c_{3,j}\, v'_{n_v+j}(t) = 0 \tag{3.37}$$

The solution of this system allows us to express the boundary nodes $i = n_v + 1, n_v + 2$ as a linear combination of the inner nodes. Similarly, the left boundary condition in Equation 3.12 leads to an expression for the nodes $i = -1, 0$

$$v'|_{x=0} = 0 \quad \Rightarrow \quad v'_0(t) = 0 \tag{3.38}$$

$$\left.\frac{\partial v'}{\partial x}\right|_{x=0} = 0 \quad \Rightarrow \quad \sum_{j=-1}^{3} d^f_{1,j}\, v'_{0+j}(t) = 0 \tag{3.39}$$

where a forward FD scheme is used for the first-order derivative approximation. Equation 3.35 together with the boundary conditions can be rewritten in compact form as

$$\dot{\mathbf{v}}(t) = \mathbf{A}\mathbf{v}(t) + \mathbf{B}_d d(t) + \mathbf{B}_u u(t) \tag{3.40}$$

where $\mathbf{B}_d = \{b_d(x_i)\},\ \mathbf{B}_u = \{b_u(x_i)\}$ and the matrix $\mathbf{A} \in \mathbb{R}^{n_v \times n_v}$ is a banded matrix.

For the time marching, the forward Euler method is used (Equation 3.41), with a CFL number of 0.05. This value was picked in order to provide a stable time marching scheme, both for the primal but also for the adjoint problem.

$$\mathbf{v}(t + \Delta t) = \mathbf{v}(t) + \Delta t[\mathbf{A}\mathbf{v}(t) + \mathbf{B}_d d(t) + \mathbf{B}_u u(t)] \tag{3.41}$$

For the non-linear equation Equation 3.7, an additional term is introduced in Equation 3.35 :

$$\begin{aligned}\frac{\mathrm{d}v'_i(t)}{\mathrm{d}t} = -V \sum_{j=-3}^{1} d^b_{1,j}\, v'_{i+j}(t) - \varepsilon\, v'_i(t) \sum_{j=-3}^{1} d^b_{1,j}\, v'_{i+j}(t) \\ - \frac{\mathcal{P}}{\mathcal{R}} \sum_{l=-2}^{2} d^c_{2,l}\, v'_{i+l}(t) - \frac{1}{\mathcal{R}} \sum_{l=-2}^{2} d^c_{4,l}\, v'_{i+l}(t) \quad + b_d(x_i)\, d(t) + b_u(x_i)\, u(t)\end{aligned} \tag{3.42}$$

The adjoint equation is discretized in the same way, both in space and time.

4

Results and Discussion

This chapter presents the findings of the study and discusses their implications in relation to the research questions introduced in Chapter 2. In particular, it addresses the research question: Can the adjoint method improve the computational efficiency of large-scale control-flow problems?

4.1 Control of the KS system using the LQR controller

The one-dimensional linearized KS equation represents an idealized approach for simulating perturbations developing within a Blasius boundary layer flow. This equation is characterized by features like convective instability, and a significant time delay. Without control, the spatiotemporal behavior of the KS equation under upstream Gaussian white noise is illustrated in Figure 4.2. This depiction shows a considerable amplification of the perturbation as it moves downstream, and the parallel slash pattern indicates the existence of a time delay. In the same figure, both the temporal noise signal with unit variance d and the output signal z at $x = 700$ are shown.

Initially, the response resembles a random signal but gradually displays characteristics of wave-like behavior. The amplitude of the disturbance grows exponentially in the x-direction due to the presence of instability within the flow. This phenomenon is illustrated in Figure 4.1, where the velocity perturbation from the final time step is shown. Furthermore, by examining d and z in Figure 4.2, it is clear that while the amplitude of perturbation increases, some frequencies are filtered by the system. This occurs because the introduction of white noise excites a wide range of frequencies, but only those associated with a specific wavelength range remain unstable and are amplified in the flow. This characteristic is typical of a convectively unstable flow, which, along with the system's nonlinearity, complicates flow control.

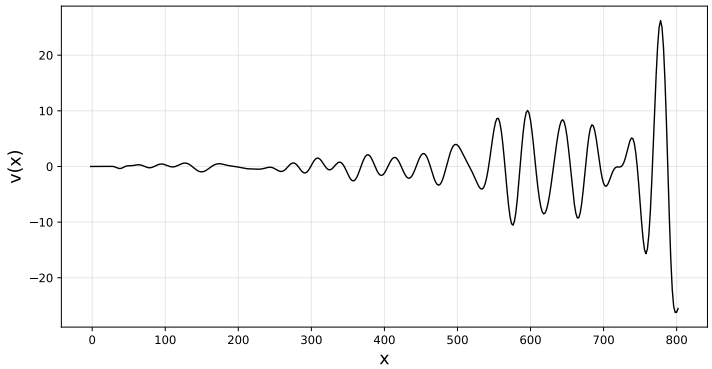

Figure 4.1: The spatial response of the system - perturbation v - on the last time step. The exponential growth is evident.

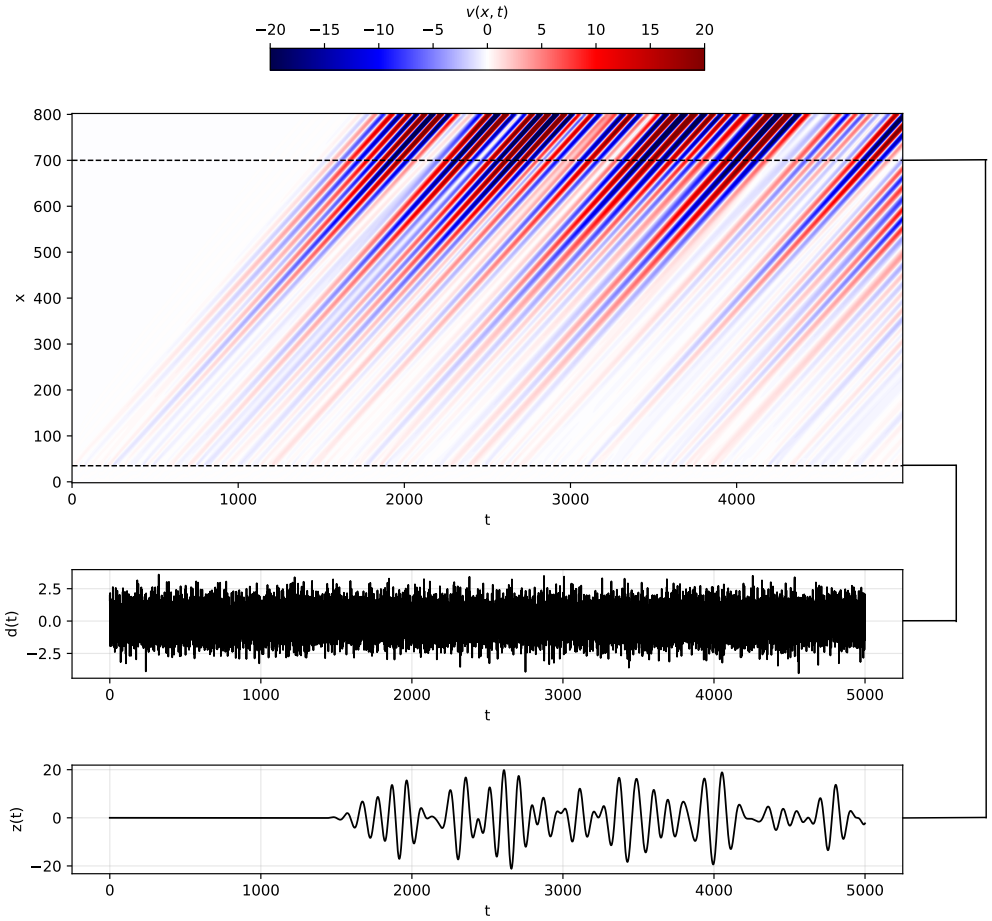

Figure 4.2: Dynamics of the 1-D linearized KS equation when subject to Gaussian white noise with unit variance: spatiotemporal response of the system; temporal signal of noise input d(t) at x = 35; output signal z(t) measured by sensor at x = 700. d is the input while z is the output

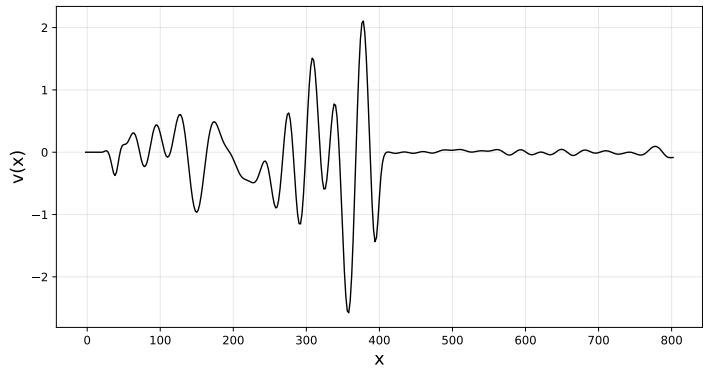

Figure 4.3: The spatial response of the system - perturbation v - on the last time step. This response includes the LQR controller which acts at x = 400.

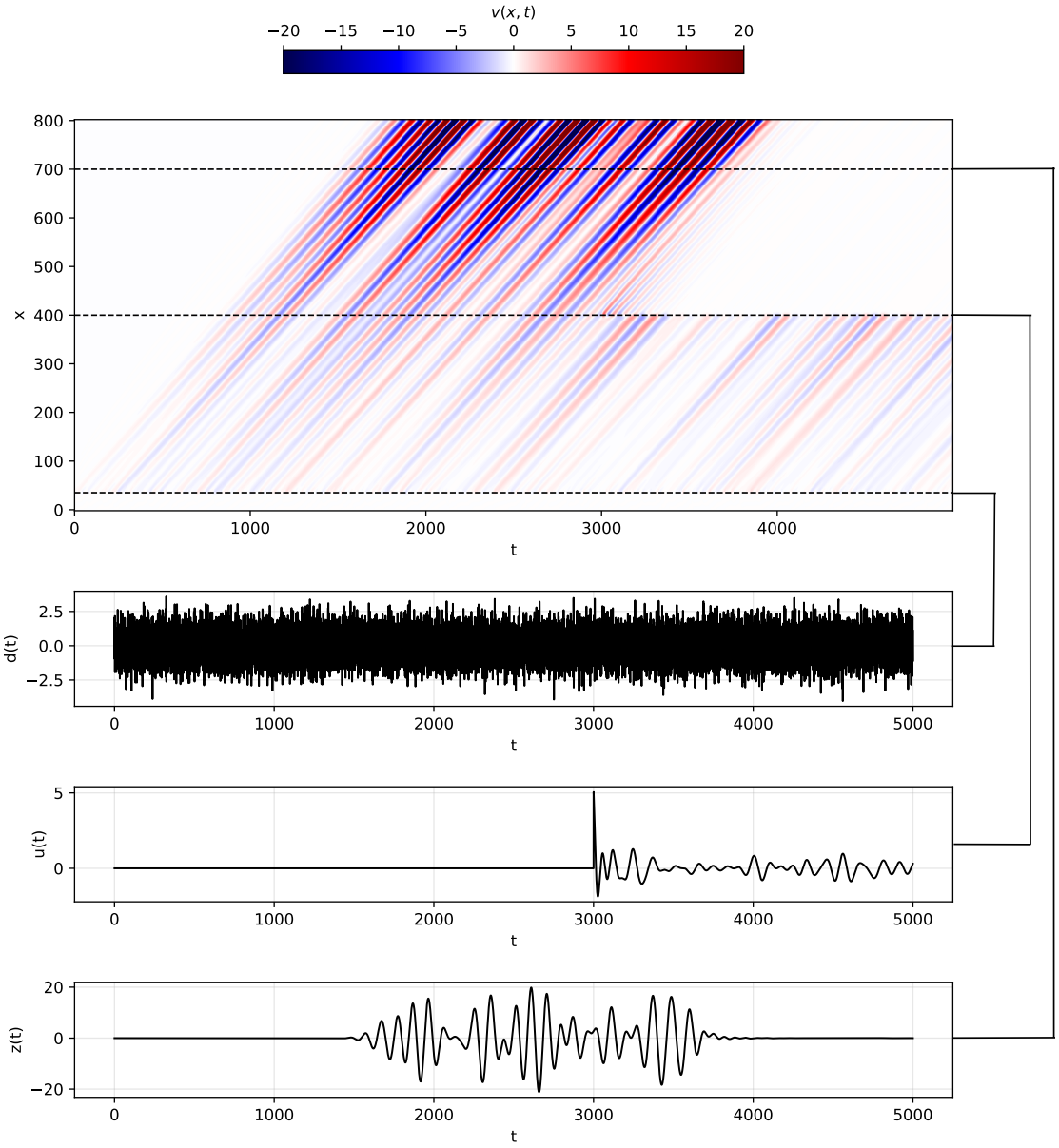

Figure 4.4: Dynamics of the 1-D linearized KS equation with both the external disturbance and control inputs: spatiotemporal response of the system; temporal signal of noise input d(t) at x = 35; temporal signal of control input u(t) at x = 400 provided by the LQR controller; output signal z(t) measured by sensor at x = 700. d and u are inputs to the system while z is the output.

4.2 Control of the linear KS system using the adjoint method

In this section the Adjoint method will be utilized with the goal of reproducing the results of the LQR controller. Figure 4.5 illustrates the response of the system to a random gaussian noise, similar to that of the previous section. The only difference here is that the axis are now flipped, with the spatial dimension x being on the horizontal axis and the temporal dimension t being on the vertical axis. This change was made for demonstrating the ability of the Adjoint method to achieve it's goal. The final time

was changed from 5000 to 2000 for better computational efficiency.

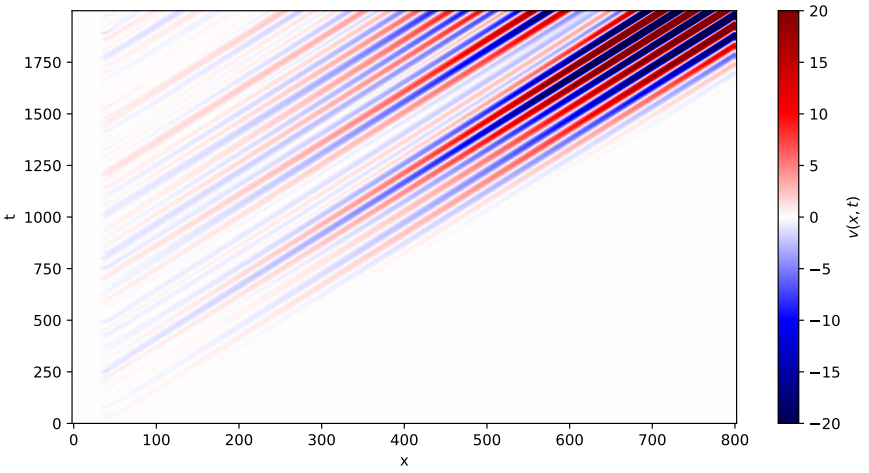

Figure 4.5: Spatiotemporal response to white noise

Figure 4.6 presents the RMS value of the perturbation v at every point in space. It is clear that although the LQR controller does not eliminate the signal, it significantly reduces it by almost to order of magnitude. In Figure 4.7 the response to the LQR control is depicted. It is important to note that the actuator at $x = 400$ is activated from the beginning, this is the reason why after that spatial point the perturbation v is almost zero for every time step.

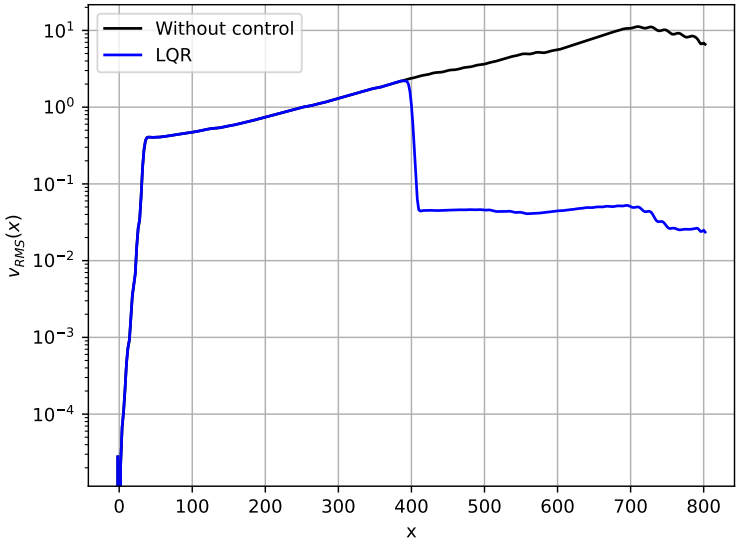

Figure 4.6: Control of the KS equation. The rms velocity as a function of the x direction is analyzed; the uncontrolled configuration is compared to the LQR controller

The reason behind this decision is the way that the objective function is defined for the adjoint problem. There, the function is an integral from the initial time ($t = 0$) to the final time ($t = T = 2000$). In this way, the gradient of the objective function that is obtained through the adjoint solution is itself a time series from 0 to 2000. This practically means that the actuator is active the whole time.

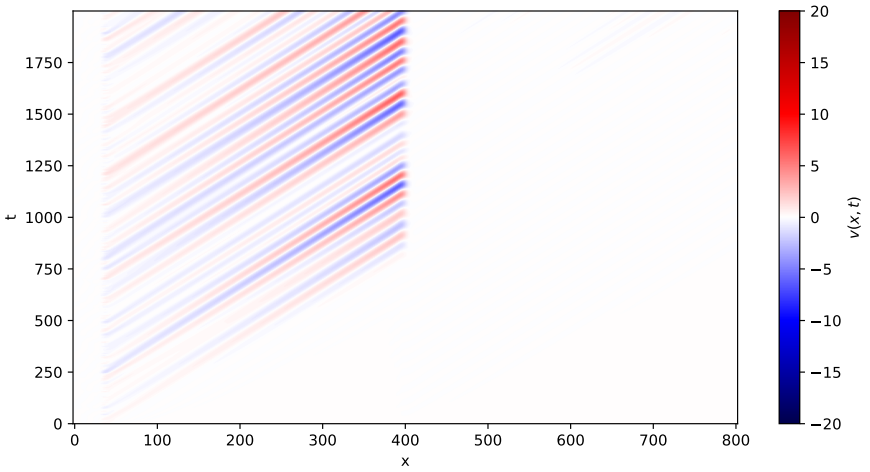

Figure 4.7: Spatiotemporal response to white noise with the LQR controller active from t=0 until t=2000

Although both the LQR and the Adjoint are based on the same principle, there is a crucial difference. The linear quadratic regulator is based on the assumption that the adjoint state p has a linear relation with the direct (or primal) state v. On top of that, the final solution for the LQR actuator comes from solving the algebraic Riccati equation. This can only happen when steady state is achieved, meaning the final time T approaches infinity ($T \to \infty$). When solving the Adjoint equation, the steady state assumption is no longer valid, as T has a district value ($T = 2000$). The effect of the violation of this assumption will be discussed in context of the optimization method that was used.

The method that was used for the optimization process is steepest descend. In Equation 3.31 learning rate μ was kept constant to the value of $1/300 \simeq 0.033$ and the total number of optimization steps was 100.

Figure 4.8 depicts the L_2 metric of the derivative of the objective function $\left\| \frac{\partial \tilde{\mathcal{L}}}{\partial u} \right\|$. The fact that after 50 iterations the slope seems to stabilize is a good indicator that the process is going to converge to a (local) optimum.

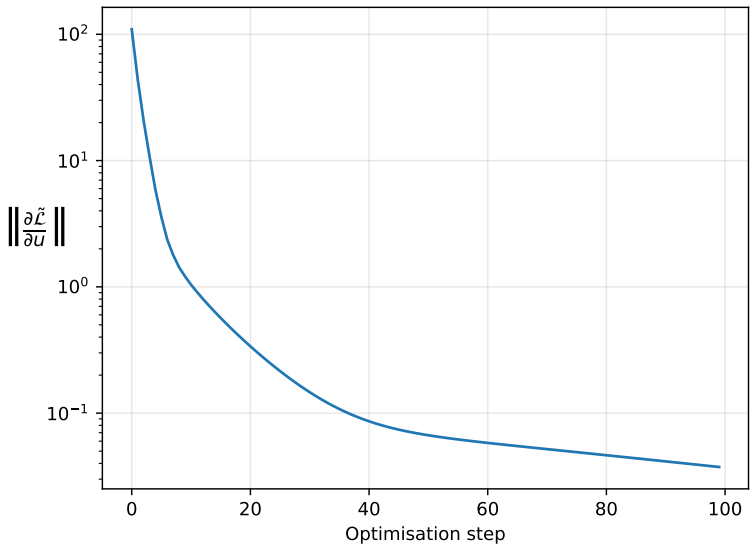

Figure 4.8: L_2 norm of the derivative of the objective function for every optimization step

Figure 4.9 illustrates the evolution of the actuator signal u. The initial guess is 0 for every time step. The first step seems to already capture the basic shape of the desired solution while the last one is almost identical to the LQR solution. This is a clear evidence that the local optimum of the optimization is the same one as that in from the Riccati solution, which is the desirable outcome. Although quite similar, the two solutions (LQR and Adjoint) present one major discrepancy: the behavior of the solution after the time $t = 1400$ (also illustrated in Figure 4.12). This effect is also clearly depicted when comparing the RMS values in Figure 4.10.

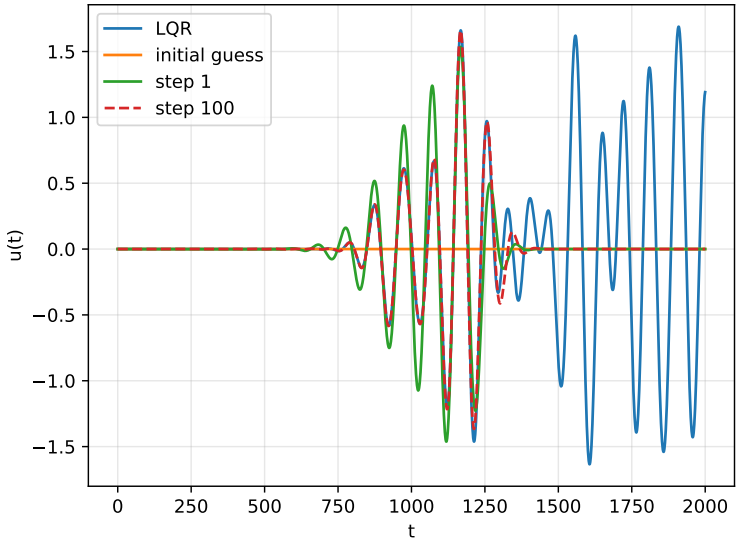

Figure 4.9: The design variable of the optimization process - the actuator signal u(t) - at the initial guess, the first and the last iteration. For comparison, the Riccati solution used in the LQR controller with the blue line.

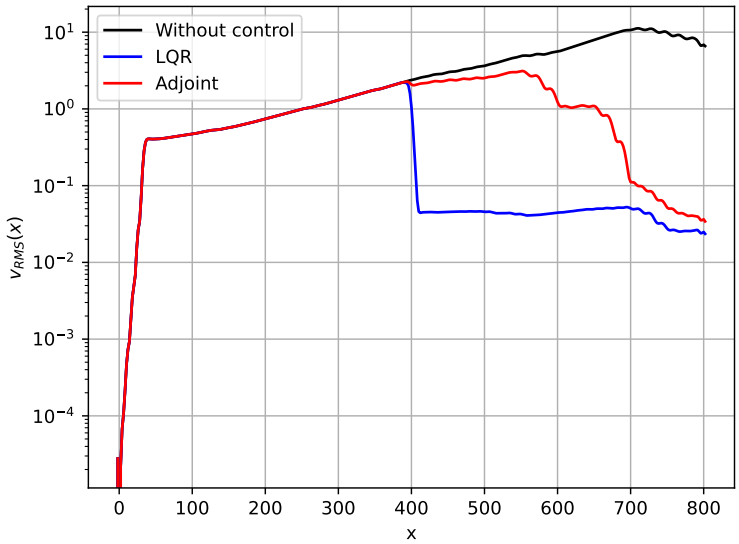

Figure 4.10: Control of the KS equation. The rms velocity as a function of the x direction is analyzed; the uncontrolled configuration is compared to the LQR controller and the solution from the optimization process using the Adjoint method

The reason behind this behavior can be explained by looking at Figure 4.11 where the time series of the

derivative of the objective function is presented. The value of the derivative is zero after $t = 1400$ because of the formulation of the objective function itself. In Equation 3.26 the velocity perturbation state vector **v** is multiplied by $\mathbf{C_z}$. This practically means that the objective function takes into consideration only the part of the state vector around the output z which is at $x = 700$. The same parameter is used in Equation 3.29 and constituently in Equation 3.30. The adjoint solution p is generated by integrating backwards in time Equation 3.29 which also include the initial condition (placed at $t = T$). As p evolves with time - here the evolution is happening backwards, from $t = T = 2000$ to $t = 0$ - at some point it passes through the actuator at $x = 400$. This time is around $t = 1400$. This clearly demonstrates the reason behind the difference with the Riccati solution, where $T \to \infty$ and thus this transient phase is considered to be infinitely far in the "future".

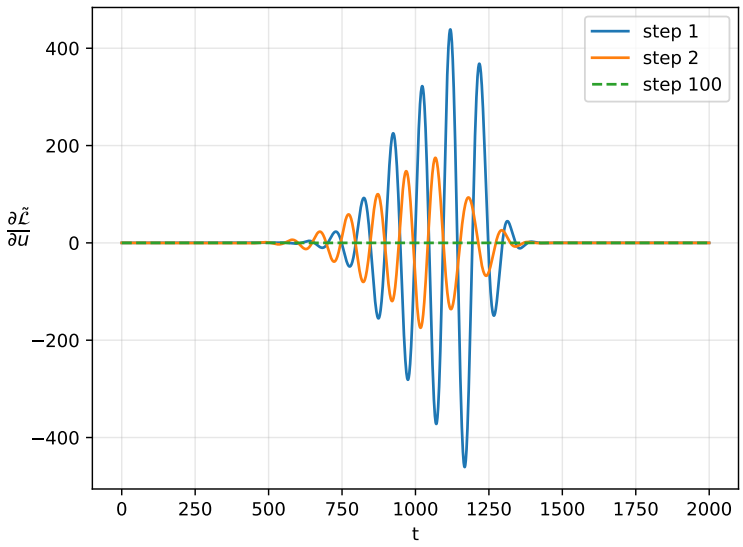

Figure 4.11: Time series of the derivative of the design variable - the actuator signal u(t) for the first, second and last optimization step

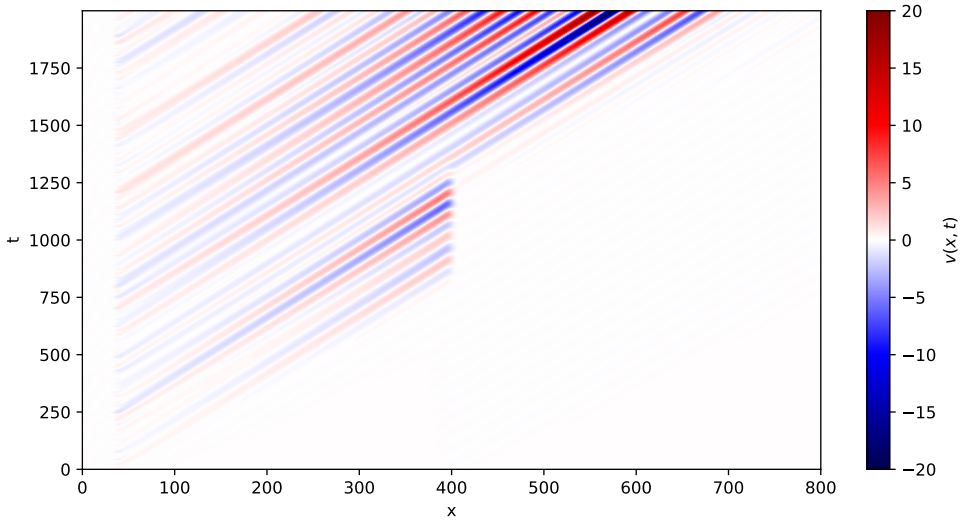

Figure 4.12: Spatiotemporal response to white noise using the solution from the optimization process which utilizes the adjoint method

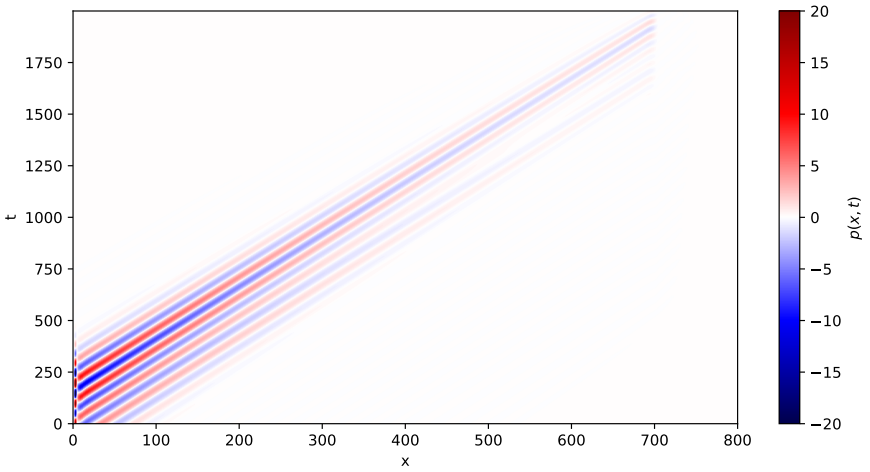

Figure 4.13: Spatiotemporal response of the adjoint variable p. The integration is done backwards, from t=2000 to t=0.

4.3 Control of the non-linear KS system using the adjoint method

The results up until this point are related to the control of the linearized KS equation. However, when the perturbation amplitude increases above a certain level, the nonlinear effect can no longer be neglected. In this section, the dynamics of the nonlinear KS equation are investigated as described by Equation 3.7 a comparison is conducted between the LQR controller and the solution provided by the Adjoint problem.

The intensity of nonlinearity depends on the value of ε. In order to study the effect of this parameter to the system, the value of ε varies from 0 to 1 with 0 corresponding to the linear equation and 1 corresponding to the fully non-linear equation. The RMS value of perturbation velocity along the 1-D domain is plotted in Figure 4.14.

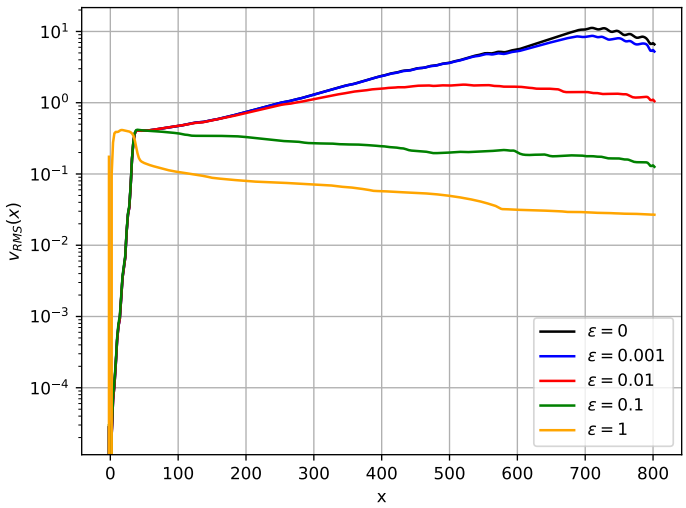

Figure 4.14: Investigation of the effect that the non-linearity has on the rms distribution of the perturbation

In the weekly nonlinear KS system ($\varepsilon = 0.001$) the response is almost identical to that of the linear one. When the ε increases though a different behavior is observed. It is shown that with the increase of ε, the nonlinear effect becomes more evident in the sense that the perturbation is no longer growing

exponentially along the x-direction, in contrast to the linear system, as shown by the black curve. Especially after the value of 0.01 the perturbation seems to be dumped. This might be correlated with the fundamental difference between the response of the linear and the non-linear system which is that the non-linearity of the equation leads to a constrained perturbation which is the opposite from what occurs in the linear case. This is also evident in Figure 4.15 were the last time step of the fully non-linear system is depicted. On the same plot, the wave accumulation pattern is observed, which is also a non-linear effect. Similar wave patterns have been observed in other non-linear systems like the Burger's equation.

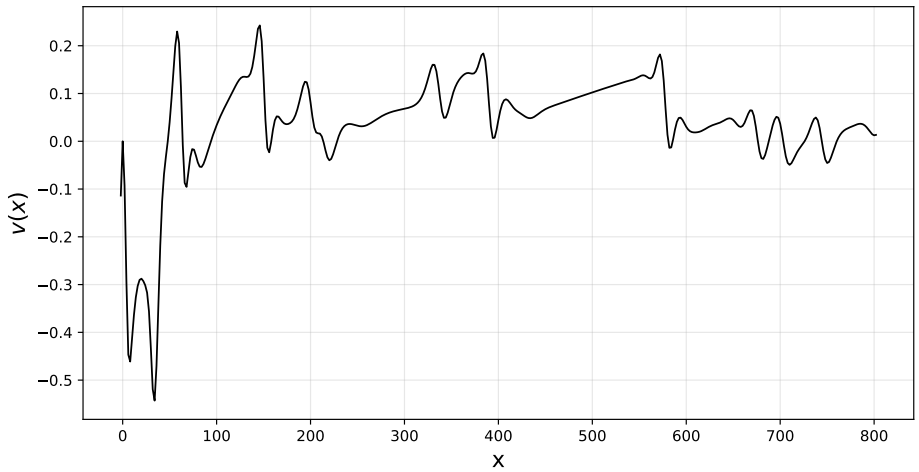

Figure 4.15: The spatial response of the non-linear system - perturbation v - on the last time step. The characteristic bounded response is evident.

Figure 4.16 presents the spatio-temporal evolution of the perturbation from the fully non-linear system ($\varepsilon = 1$). One difference that has not been discussed already is the bifurcations that occur at the point of the disturbance ($x = 35$).

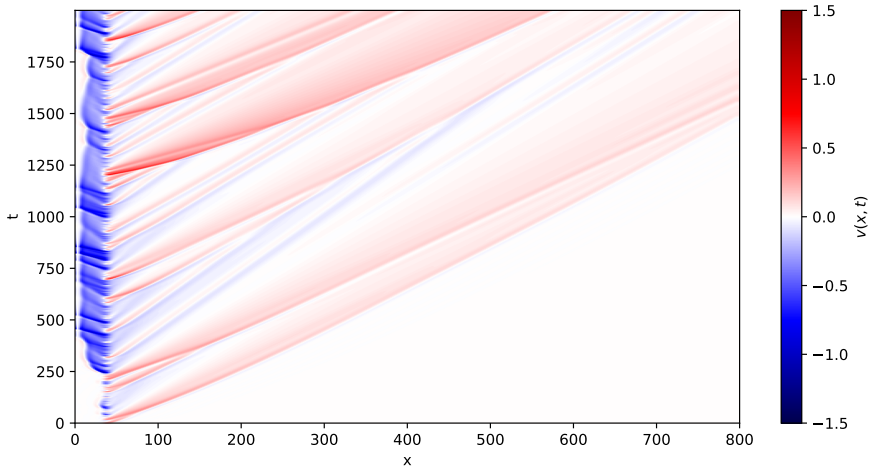

Figure 4.16: Spatiotemporal response of the non-linear system to white noise

In that particular area a splitting behavior occurs where some waves travel to the right and some to the left. This is expected, as the non-linear system enables this kind of propagation, as the sign of the

perturbation affects the propagation direction. This is also verified by the ”bump” in Figure 4.14 that is observed between the values $x = 0$ and $x = 35$.

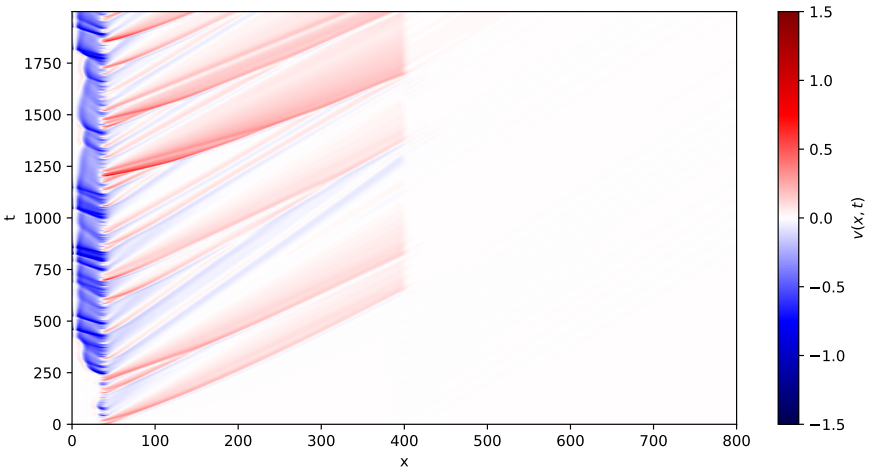

Figure 4.17: Spatiotemporal response of the non-linear system to white noise with the LQR controller active from t=0 until t=2000

Figure 4.17 depicts the spatio-temporal perturbation response to the non-linear system using the LQR controller - the solution to the Ricccati equation. The first assumption of the LQR controller is that the adjoint state p is in linearly related to the state variable v - which might not be the case in the non-linear equation. Despite this fact, it seems that it works also for the non-linear case as it achieves its goal which is the reduction of the perturbation. This can be also verified by looking at the RMS values in Figure 4.20.

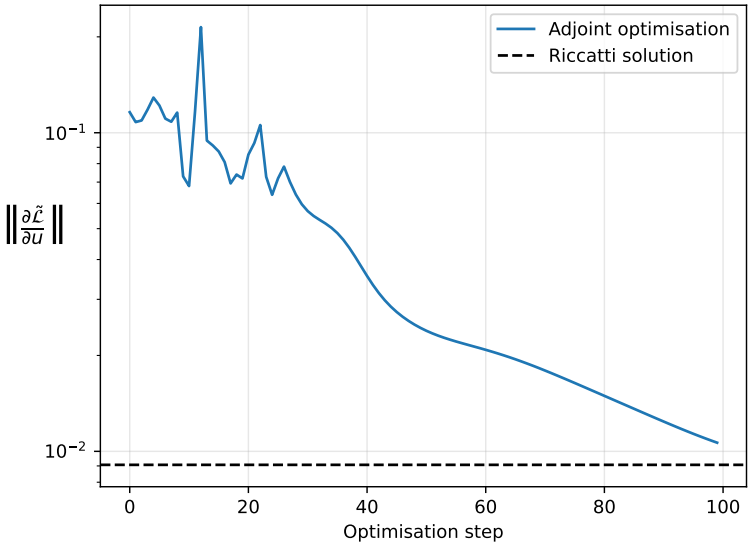

Figure 4.18: L_2 norm of the derivative of the objective function for every optimization step for the non-linear system. The reduction of the value of the learning rate at the 25th step produces a smoother curve.

Regarding the optimization method for the non-linear equation the steepest decent method was also used. The learning rate μ was kept constant to the value of $5e-3$ until step 25 and at $5e-4$ afterwards.

This was done in order to help the algorithm to find a smaller minimum, as taking smaller ”steps” leads to a more refined solution. The difference is also seen in the behavior of the L_2 norm of the derivative of the objective function, shown in Figure 4.18, as the curve after the 25^{th} step becomes smoother. The total number of optimization steps was 100.

The final solution of the optimization process is illustrated in Figure 4.19. The RMS curves in Figure 4.20 have a similar behavior with the corresponding curves in the linear case, meaning the Adjoint curve lies between the ”Without control” and LQR curves. This is due to the fact that the gradient that is calculated through the adjoint variable p has zero values in the time interval after 1400 Figure 4.23, just like the linear case.

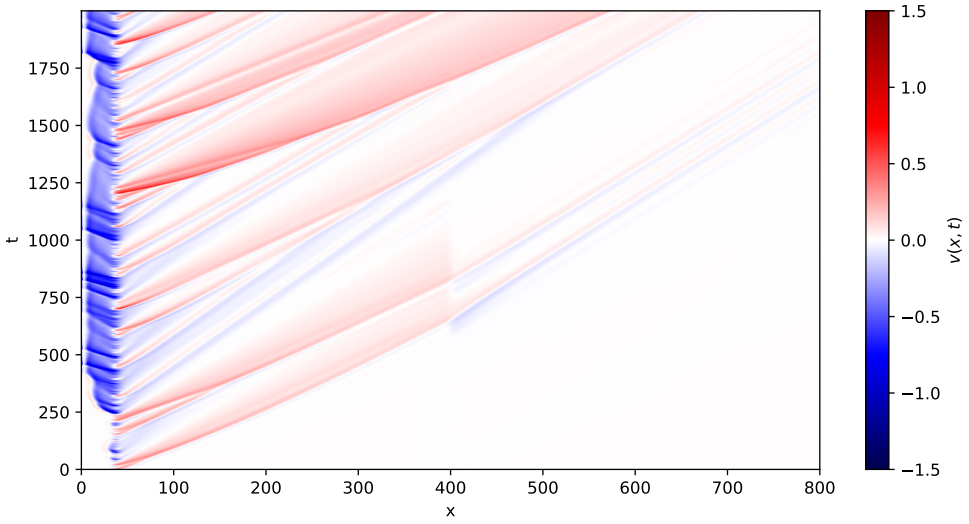

Figure 4.19: Spatiotemporal response of the non-linear system to white noise using the solution from the optimization process which utilizes the adjoint method

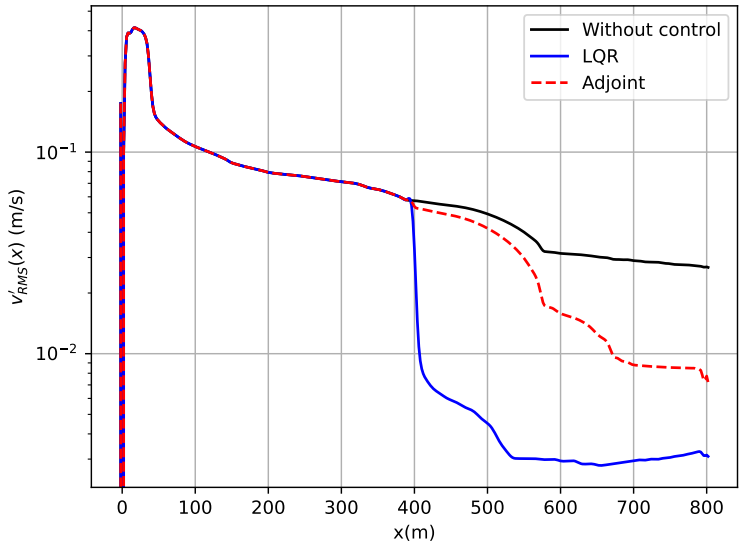

Figure 4.20: Control of the non-linear KS equation. The rms velocity as a function of the x direction is analyzed; the uncontrolled configuration is compared to the LQR controller and the solution from the optimization process using the Adjoint method

The optimization solution for the actuator signal time series $u(t)$ is presented in Figure 4.22. Contrary to the linear case, this time the algorithm cannot capture the exact shape of the Riccati solution - the red dotted curve agrees partially with the blue curve. In order to check how close there two curves are - assuming the Riccati solution is the ideal - the value of the derivative of the objective function that corresponds to the Riccati solution is plotted in Figure 4.18. There, it's clear that the optimization process that uses the adjoint state for calculating the derivative of the objective function "converges" to the Riccati solution, at least from the perspective of the L_2 metric. This is a great indicator that the Adjoint method is as effective as solving the Riccati equation.

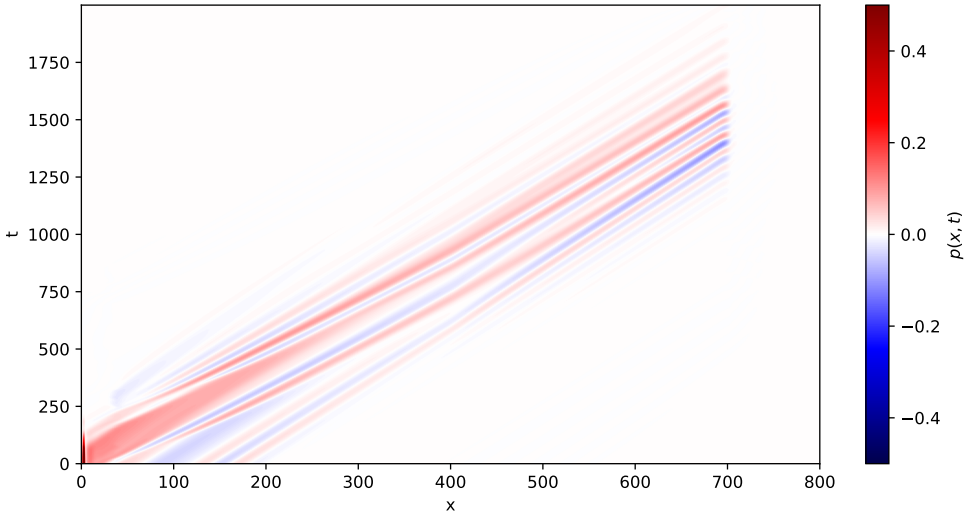

Figure 4.21: Spatiotemporal response of the adjoint variable p for the non-linear system. The integration is done backwards, from t=2000 to t=0.

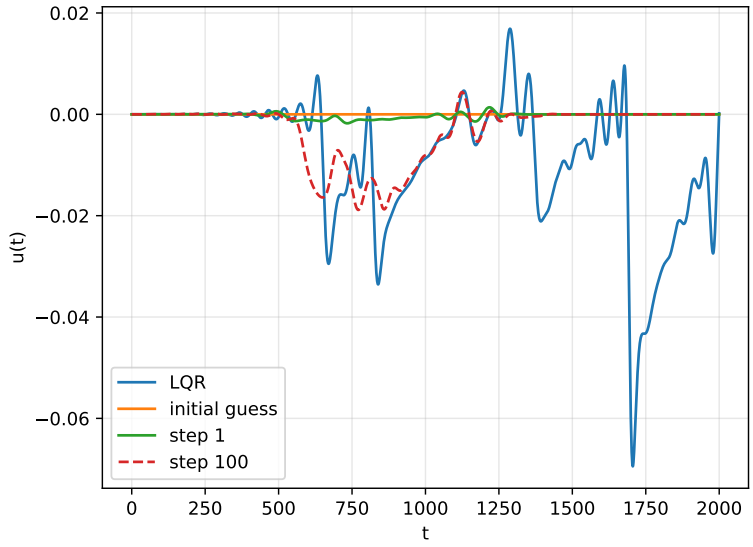

Figure 4.22: The design variable of the optimization process - the actuator sugnal u(t) - at the initial guess, the first and the last iteration. For comparison, the Riccati solution used in the LQR controller with the blue line.

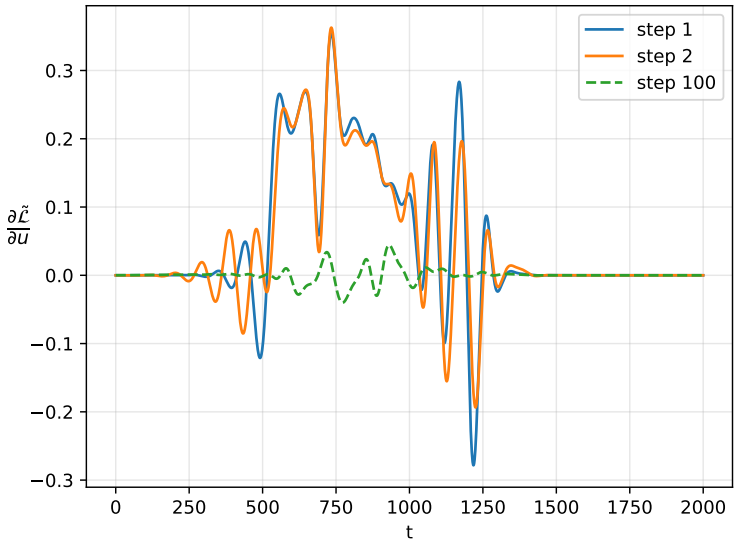

Figure 4.23: Non-linear KS equation: Time series of the derivative of the design variable - the actuator signal u(t) for the first, second and last optimization step.

In low-dimensional systems ($n_v < 10^3$), someone can find Riccati equation solvers in standard software packages. However, for larger systems ($n_v > 10^3$), as the ones encountered in flow control studies, direct methods become impractical. This is because the Riccati equation solution forms a full matrix, requiring storage on the order of at least $\mathcal{O}(n_v^2)$. This is were the adjoint method cen provide a solution.

The adjoint technique can reproduce the results of the Riccati equation - as it was demonstrated in this chapter - not only for the linear but also for the non-linear KS equation. The effectiveness in the non-linear case is crucial, as the full Navier-Stokes equations are also non-linear.

The computational cost for solving the Riccati equation is $\mathcal{O}(n_v^3)$ [30]. For acquiring the same solution through the adjoint method, one should take into consideration the cost for the primal and the adjoint problem. Both of them have the computational cost of $\mathcal{O}(n_v^2)$, when using an explicit temporal scheme - this can be improved by using higher order schemes that lead to larger values for the CFL number and thus faster time marching. It is clear that the adjoint method is far less expensive, especially in large scale systems. One drawback of the method is the large memory needs when dealing with non-linear systems as the NS equations. There the whole state matrix has to be stored for each time step.

In order to mitigate this memory problem, methods like the ”Checkpointing Algorithm” have been invented. There, the solution is saved only up to a certain time step. Then, when the adjoint problem is solved and the - backwards in time - integration is conducted, the solution is re-calculated until the time step that is needed. Some algorithms [31] can provide extra advantages like no need of knowing beforehand the number of time steps; minizing the number of recalculations and being able to integrate an arbitrary number of time steps. Future work building on this thesis could focus on combining the adjoint method with an efficient memory management algorithm and applying it to more realistic models, such as the full nonlinear Navier–Stokes equations.

In summary, the adjoint method along with efficient and smart algorithms (like checkpointing) is an efficient computational tool for large scale control-flow problems as it reduces the cost both in time and in memory.

References

[1] D. M. Bushnell and J. N. Hefner, *Viscous drag reduction in boundary layers*, Jan. 1, 1990.

[2] H. Schlichting and K. Gersten, *Boundary-Layer Theory*. Berlin, Heidelberg: Springer Berlin Heidelberg, 2017, ISBN: 978-3-662-52917-1 978-3-662-52919-5. DOI: 10.1007/978-3-662-52919-5.

[3] G. S. Schairer, "Some opportunities for progress in aircraft performance. iii," *Journal of Aircraft*, vol. 1, no. 2, pp. 49–70, Mar. 1964, ISSN: 0021-8669. DOI: 10.2514/3.27731.

[4] J. Kim and T. R. Bewley, "A linear systems approach to flow control," *Annual Review of Fluid Mechanics*, vol. 39, no. 1, pp. 383–417, Jan. 1, 2007, ISSN: 0066-4189, 1545-4479. DOI: 10.1146/annurev.fluid.39.050905.110153.

[5] M. Gad-el-Hak, *Flow Control: Passive, Active, and Reactive Flow Management*. Cambridge: Cambridge University Press, 2000, ISBN: 978-0-521-77006-4. DOI: 10.1017/CBO9780511529535.

[6] Y. Kuramoto and T. Tsuzuki, "Persistent propagation of concentration waves in dissipative media far from thermal equilibrium," *Progress of Theoretical Physics*, vol. 55, no. 2, pp. 356–369, Feb. 1, 1976, ISSN: 0033-068X. DOI: 10.1143/PTP.55.356.

[7] G. I. Sivashinsky, "Nonlinear analysis of hydrodynamic instability in laminar flames—i. derivation of basic equations," *Acta Astronautica*, vol. 4, no. 11, pp. 1177–1206, Nov. 1, 1977, ISSN: 0094-5765. DOI: 10.1016/0094-5765(77)90096-0.

[8] "Lewis, f.l. and syrmos, v.l. (1995) optimal control. 2nd edition, john wiley & sons, new york, 315. - references - scientific research publishing," Accessed: Sep. 7, 2025. [Online]. Available: https://www.scirp.org/reference/referencespapers?referenceid=2464723.

[9] M. M. F. D. Oliveira, N. F. F. Ebecken, J. L. F. D. Oliveira, and M. Aires, "Numerical modeling of air pollutants emitted by waterway transportation," *Journal of Geoscience and Environment Protection*, vol. 04, no. 6, pp. 123–136, 2016, ISSN: 2327-4336, 2327-4344. DOI: 10.4236/gep.2016.46011.

[10] G. E. A. Meier, "Active control of boundary layer and separation," in *Control of Flow Instabilities and Unsteady Flows*, G. E. A. Meier and G. H. Schnerr, Eds., Vienna: Springer, 1996, pp. 203–233, ISBN: 978-3-7091-2688-2. DOI: 10.1007/978-3-7091-2688-2_5.

[11] J. P. Robert, "Drag reduction: An industrial challenge," in *Special Course on Skin Friction Drag Reduction*, ser. AGARD Report, J. Cousteix, Ed., vol. 786, AGARD, Mar. 1992, pp. 2–13.

[12] D. M. Bushnell and K. J. Moore, "Drag reduction in nature,"

[13] J. D. Anderson, *Fundamentals of aerodynamics* (McGraw-Hill series in aeronautical and aerospace engineering), Sixth edition. New York, NY: McGraw-Hill Education, 2017, 1130 pp., ISBN: 978-1-259-12991-9.

[14] S. Bagheri and D. S. Henningson, "Transition delay using control theory," *Philosophical Transactions of the Royal Society A: Mathematical, Physical and Engineering Sciences*, vol. 369, no. 1940, pp. 1365–1381, Apr. 13, 2011. DOI: 10.1098/rsta.2010.0358.

[15] J. H. Fransson, "Transition to turbulence delay using a passive flow control strategy," *Procedia IUTAM*, vol. 14, pp. 385–393, 2015, ISSN: 22109838. DOI: 10.1016/j.piutam.2015.03.018.

[16] J. M. Burgers, "The motion of a fluid in the boundary layer along a plain smooth surface," in *Proceedings of the First International Congress for Applied Mechanics*, Delft, 1924, pp. 113–128.

[17] B. G. Van der Hegge Zijnen, "Measurements of the velocity distribution in the boundary layer along a plane surface," Thesis, Delft University of Technology, Delft, 1924.

[18] P. J. Schmid and D. S. Henningson, *Stability and Transition in Shear Flows* (Applied Mathematical Sciences). New York, NY: Springer, 2001, ISBN: 978-1-4612-6564-1 978-1-4613-0185-1. DOI: 10.1007/978-1-4613-0185-1.

[19] M. R. Jovanović and B. Bamieh, "Componentwise energy amplification in channel flows," *Journal of Fluid Mechanics*, vol. 534, pp. 145–183, Jul. 2005, ISSN: 1469-7645, 0022-1120. DOI: 10.1017/S0022112005004295.

[20] P. J. Schmid, "Nonmodal stability theory," *Annual Review of Fluid Mechanics*, vol. 39, no. 1, pp. 129–162, Jan. 1, 2007, ISSN: 0066-4189, 1545-4479. DOI: 10.1146/annurev.fluid.38.050304.092139.

[21] S. S. Joshi, J. L. Speyer, and J. Kim, "A systems theory approach to the feedback stabilization of infinitesimal and finite-amplitude disturbances in plane poiseuille flow," *Journal of Fluid Mechanics*, vol. 332, pp. 157–184, Feb. 1997, ISSN: 0022-1120, 1469-7645. DOI: 10.1017/S0022112096003746.

[22] T. R. Bewley and S. Liu, "Optimal and robust control and estimation of linear paths to transition," *Journal of Fluid Mechanics*, vol. 365, pp. 305–349, Jun. 25, 1998, ISSN: 0022-1120, 1469-7645. DOI: 10.1017/s0022112098001281.

[23] M. Chevalier, J. Hœpffner, E. Åkervik, and D. S. Henningson, "Linear feedback control and estimation applied to instabilities in spatially developing boundary layers," *Journal of Fluid Mechanics*, vol. 588, pp. 163–187, Oct. 2007, ISSN: 1469-7645, 0022-1120. DOI: 10.1017/S0022112007007392.

[24] A. Monokrousos, L. Brandt, P. Schlatter, and D. S. Henningson, "DNS and LES of estimation and control of transition in boundary layers subject to free-stream turbulence," *International Journal of Heat and Fluid Flow*, vol. 29, no. 3, pp. 841–855, Jun. 2008, ISSN: 0142-727X. DOI: 10.1016/j.ijheatfluidflow.2008.03.009.

[25] R. W. Milling, "Tollmien–schlichting wave cancellation," *The Physics of Fluids*, vol. 24, no. 5, pp. 979–981, May 1, 1981, ISSN: 0031-9171. DOI: 10.1063/1.863471.

[26] N. Goldin, R. King, A. Pätzold, W. Nitsche, D. Haller, and P. Woias, "Laminar flow control with distributed surface actuation: Damping tollmien-schlichting waves with active surface displacement," *Experiments in Fluids*, vol. 54, no. 3, p. 1478, Mar. 15, 2013, ISSN: 1432-1114. DOI: 10.1007/s00348-013-1478-6.

[27] L. I. Cerviño and T. R. Bewley, "On the extension of the complex-step derivative technique to pseudospectral algorithms," *Journal of Computational Physics*, vol. 187, no. 2, pp. 544–549, May 20, 2003, ISSN: 0021-9991. DOI: 10.1016/S0021-9991(03)00123-2.

[28] "(PDF) dissipative structures and weak turbulence," *ResearchGate*, Aug. 10, 2025. DOI: 10.1007/3-540-60188-0_59.

[29] "Active cancellation of artificially introduced tollmien–schlichting waves using plasma actuators | request PDF," *ResearchGate*, Aug. 9, 2025. DOI: 10.1007/s00348-007-0436-6.

[30] P. Van Dooren, "A generalized eigenvalue approach for solving riccati equations," *SIAM Journal on Scientific and Statistical Computing*, vol. 2, no. 2, pp. 121–135, Jun. 1981, ISSN: 0196-5204. DOI: 10.1137/0902010.

[31] Q. Wang, P. Moin, and G. Iaccarino, "Minimal repetition dynamic checkpointing algorithm for unsteady adjoint calculation," *SIAM*, Jun. 2009, ISSN: 1064-8275.